J|A|C|S
ARTICLES
Published on Web 06/22/2004

Nature of the Peroxo Intermediate of the W48F/D84E Ribonucleotide Reductase Variant: Implications for O_2 Activation by Binuclear Non-Heme Iron Enzymes

Andrew J. Skulan,[†] Thomas C. Brunold,[†,§] Jeffrey Baldwin,[‡] Lana Saleh,[‡] J. Martin Bollinger, Jr.,*[,‡] and Edward I. Solomon*[,†]

Contribution from the Department of Chemistry, Stanford University, Stanford, California 94305, and Department of Biochemistry and Molecular Biology, The Pennsylvania State University, University Park, Pennsylvania 16802

Received February 18, 2004; E-mail: Edward.Solomon@stanford.edu; jmb21@psu.edu

Abstract: Analysis of the spectroscopic signatures of the R2-W48F/D84E biferric peroxo intermediate identifies a *cis* μ-1,2 peroxo coordination geometry. DFT geometry optimizations on both R2-W48F/D84E and R2-wild-type peroxo intermediate models including constraints imposed by the protein also identify the *cis* μ-1,2 peroxo geometry as the most stable peroxo intermediate structure. This study provides significant insight into the electronic structure and reactivity of the R2-W48F/D84E peroxo intermediate, structurally related *cis* μ-1,2 peroxo model complexes, and other enzymatic biferric peroxo intermediates.

1. Introduction

Ribonucleotide reductase (RR) performs the final step in deoxyribonucleotide biosynthesis, catalyzing the reduction of ribonucleotides to deoxyribonucleotides and is thus essential to DNA biosynthesis.[1,2] Subunit R2 of this protein contains a diiron center which activates dioxygen to produce a long-lived tyrosyl radical, Y122$^{\bullet}$, which, in turn, accepts an electron from the active site of R1 in the first step of nucleotide reduction. Other members of the class of binuclear non-heme iron enzymes activate O_2 in order to perform a wide range of oxidation chemistries, including methane monooxygenase (MMO), which oxidizes methane to methanol,[3] and stearoyl-acyl carrier protein Δ^9-desaturase (Δ9D), which inserts a double bond into stearoyl-ACP between C_9 and C_{10} during fatty acid biosynthesis.[4,5]

The binuclear iron sites in biferrous RR, MMO, and Δ9D are quite similar. MMO[6,7] and Δ9D[8] possess two bridging glutamates, as well as a terminal histidine and bidentate glutamate residue coordinating each of the irons (a $Fe_2(Glu)_4(His)_2$ site), while RR has one of the terminal glutamates replaced by a chemically similar aspartate (D84) to create an $Fe_2(Glu)_3(Asp)(His)_2$ site.[9,10] D84 is located adjacent to radical-forming Y122. The similarities in coordinating residues in RR, MMO, and Δ9D do not extend to the second coordination sphere, with the hydrogen-bonding residues that orient the coordinating residues in specific geometries differing between these three proteins.[8,11,12] Thus, while the general structural motif of the diiron active site is preserved, the relative energetics of different oxygen intermediate structures may vary between these enzymes.

To better understand the origins of the reactivity of wild-type (wt) RR and its relationship to other members of the binuclear non-heme iron class, a series of amino acid substitutions were made to residues surrounding the R2 active site or involved in the electron-transfer pathway linking the catalytic active site in R1 to the binuclear iron site in R2.[13−18] Two of these pertain to this study: R2-D84E [17] and R2-W48F/D84E.[18] The single variant changes the active site ligation to become homologous to those of MMO and Δ9D ($Fe_2(Glu)_4(His)_2$), while the double variant also changes an additional residue in the electron-transfer chain linking the active sites of R1 and R2 and is believed to alter the reaction kinetics of the enzyme, as described below.

[†] Stanford University.
[‡] Pennsylvania State University.
[§] Current address: Department of Chemistry, University of Wisconsin, Madison, WI 53706.

(1) Reichard, P.; Ehrenberg, A. *Science* **1983**, *221*, 514−519.
(2) Solomon, E. I.; Brunold, T. C.; Davis, M. I.; Kemsley, J. N.; Lee, S. K.; Lehnert, N.; Neese, F.; Skulan, A. J.; Yang, Y. S.; Zhou, J. *Chem. Rev.* **2000**, *100*, 235−349.
(3) Wallar, B. J.; Lipscomb, J. D. *Chem. Rev.* **1996**, *96*, 2625−2658.
(4) Wada, H.; Schmidt, H.; Heinz, E.; Murata, N. *J. Bacteriology* **1983**, *175*, 544−547.
(5) Schmidt, H.; Heinz, E. *Plant Physiol.* **1990**, *94*, 214−220.
(6) Elango, N.; Radhakrishnan, R.; Froland, W.; Wallar, B.; Earhart, C.; Lipscomb, J.; Ohlendorf, D. *Protein Sci.* **1997**, *6*, 556−568.
(7) Rosenzweig, A.; Nordlund, P.; Takahara, P.; Frederick, C.; Lippard, S. *Chem. Biol.* **1995**, *2*, 409−418.
(8) Lindqvist, Y.; Huang, W.; Schneider, G.; Shanklin, J. *EMBO J.* **1996**, *15*, 4081−4092.
(9) Nordlund, P.; Sjoberg, B.; Eklund, H. *Nature* **1990**, *345*, 593−598.
(10) Nordlund, P.; Eklund, H. *J. Mol. Biol.* **1993**, *232*, 123−164.
(11) Lovell, T.; Li, J.; Noodleman, L. *Inorg. Chem.* **2001**, *40*, 5267−5278.
(12) Lovell, T.; Li, J.; Noodleman, L. *J. Biol. Inorg. Chem.* **2002**, *7*, 799−809.
(13) Parkin, S.; Chen, S.; Ley, B.; Mangravite, L.; Edmondson, D.; Huynh, B.; Bollinger, J. *Biochemistry* **1998**, *37*, 1124−1130.
(14) Baldwin, J.; Moenne-Loccoz, P.; Krebs, C.; Ley, B.; Edmondson, D.; Huynh, B.; Loehr, T.; Bollinger, J. *J. Inorg. Biochem.* **1999**, *74*, 74.
(15) Baldwin, J.; Krebs, C.; Ley, B.; Edmondson, D.; Huynh, B.; Bollinger, J. *J. Am. Chem. Soc.* **2000**, *122*, 12195−12206.
(16) Krebs, C.; Davydov, R.; Baldwin, J.; Hoffman, B.; Bollinger, J.; Huynh, B. *J. Am. Chem. Soc.* **2000**, *122*, 5327−5336.
(17) Bollinger, J. M.; Krebs, C.; Vicol, A.; Chen, S. X.; Ley, B. A.; Edmondson, D. E.; Huynh, B. H. *J. Am. Chem. Soc.* **1998**, *120*, 1094−1095.
(18) Moenne-Loccoz, P.; Baldwin, J.; Ley, B.; Loehr, T.; Bollinger, J. *Biochemistry* **1998**, *37*, 14659−14663.

10.1021/ja049106a CCC: $27.50

A biferric peroxo intermediate has not been definitively identified in R2-wt. Upon addition of O_2 to biferrous R2-wt, a "diradical state" forms, consisting of $W48^{+\bullet}$ (a tryptophan cation radical) and the $S = {}^1/_2$, high-valent iron-oxo intermediate, **X**.[15,19] Formation of **X** involves cleavage of the O−O bond and forms what is described as an $Fe^{III}Fe^{IV}$ dimer in either a bis-μ-oxo[20] or, more likely, a mono-μ-oxo,[21] terminal OH_x structure.[20,22] **X** decays to form $Y122^{\bullet}$ and a μ-oxo-biferric iron site. The R2-D84E variant forms a biferric peroxo intermediate ($t_{1/2} = 0.7$ s at 5 °C) when oxygen is added to its biferrous form.[17] The R2-D84E peroxo intermediate does not lead to accumulation of **X** but instead generates the signatures of a biferric iron site and tyrosine radical, suggesting that the D84E substitution has changed the kinetics of the enzyme to allow the peroxo to accumulate, but not **X**, in contrast to R2-wt. The double variant, R2-W48F/D84E, also forms a biferric peroxo intermediate ($t_{1/2} = 2.7$ s at 5 °C) but forms neither **X** nor $Y122^{\bullet}$.[18] R2-W48F/D84E is observed to self-hydroxylate at F208, a reaction that is believed to be a consequence of both the D84E mutation, which changes the coordinating ligand set to match that of MMO, and the W48F mutation, which blocks electron transfer from the binuclear site and, thus, prevents the formation of **X**. The partially activated oxygen adduct (i.e., the peroxo intermediate) is then able to react along a different, slower pathway, possibly analogous to that of MMO, to self-hydroxylate.

The first step in oxygen activation in binuclear non-heme iron enzymes is dioxygen reacting with a biferrous site to form a biferric peroxo intermediate. The peroxo intermediate of MMO, **P**, displays an intense absorption feature at ~700 nm ($\epsilon = \sim 2000\ M^{-1}\ cm^{-1}$)[23,24] and a Mössbauer doublet ($\delta = 0.67$ mm s^{-1}, $\Delta E_Q = 1.51$ mm s^{-1}) consistent with a biferric species.[25,26] The most recent computational studies propose a μ-η^2:η^2 peroxo coordination geometry for this intermediate.[27,28]

Δ9D-peroxo is more stable, allowing absorption ($\lambda = \sim 700$ nm, $\epsilon = 1200\ M^{-1}\ cm^{-1}$),[29] Mössbauer (two doublets identified; $\delta = 0.68$ mm s^{-1}, $\Delta E_Q = 1.90$ mm s^{-1} and $\delta = 0.64$ mm s^{-1}, $\Delta E_Q = 1.06$ mm s^{-1})[30] and resonance Raman (rR) (ν(Fe−O) = 442 cm^{-1}, ν(O−O) = 898 cm^{-1})[31] data to be obtained. Analysis of these data suggested a μ-1,2 peroxo coordination mode based upon comparison to spectroscopic features of well-characterized model complexes.[32]

Although no experimental evidence exists for a peroxo intermediate in R2-wt, computational studies have proposed that this species would be a μ-η^2:η^2 peroxo intermediate similar to that of MMO.[28] The R2-D84E peroxo intermediate has an absorption peak at 700 nm ($\epsilon = 1500\ M^{-1}\ cm^{-1}$) and Mössbauer parameters similar to those of the MMO peroxo intermediate ($\delta = 0.63$ mm s^{-1}, $\Delta E_Q = 1.58$ mm s^{-1}).[17] Corresponding data for the R2-W48F/D84E peroxo intermediate are absorption ($\lambda = 700$ nm, $\epsilon = 1800\ M^{-1}cm^{-1}$)[33] and Mössbauer ($\delta = 0.65$ mm s^{-1}, $\Delta E_Q = 1.63$ mm s^{-1} and $\delta = 0.61$ mm s^{-1}, $\Delta E_Q = 1.48$ mm s^{-1}).[34] R2-wt and R2-D84E have parallel reactivities, with both forming $Y122^{\bullet}$, while the similarities in the biferrous crystal structures of R2-D84E and R2-W48F/D84E and spectroscopic signatures of their peroxo intermediates suggest that these two species have the same active site structure. Clearly, spectroscopic data are best obtained on the R2-peroxo intermediate of the variant that accumulates the most peroxo intermediate, which prompted us to select the R2-W48F/D84E peroxo intermediate as the focus of this study.

Ever-increasing computational power has allowed progressively larger models of protein active sites to be constructed to investigate enzymatic catalysis. In recent studies on R2[35] and MMO,[27,36] this has allowed the diiron active site to be modeled by truncating the six iron-coordinating residues at their α-carbon positions and including models of the second coordination sphere residues that interact most strongly (both electrostatically and sterically) with the coordinating residues. These additions greatly improved the agreement between geometry optimized biferrous and biferric computational models and the corresponding X-ray crystal structures.

The results of parallel spectroscopic and computational investigations have defined the geometries of the biferrous R2-W48F/D84E (Chart 1a) and R2-wt (Chart 1b) proteins.[35] Both possess one four-coordinate (4C) and one five-coordinate (5C) iron, although the identity of the 5C iron changes between the two proteins. For R2-W48F/D84E, Fe1 is 5C, singly coordinated to E115, H118, and E238 and bidentate to E84. Fe2 is 4C and is singly coordinated to E115, E204, E238, and H241. The R2-wt has similar ligation, except D84 is monodentate to Fe1 and E204 is bidentate to Fe2, resulting in the change from (5C, 4C) in the R2-W48F/D84E variant to (4C, 5C) in R2-wt. This change is due to the lengthening of the R-group of residue 84 in the R2-W48F/D84E variant by one methylene unit relative to R2-wt which forces the E84 carboxylate into a bidentate coordination mode. This change in coordination number on Fe1 propagates through the μ-1,3 carboxylate bridges leading to a monodentate coordination mode of E204 and a 4C Fe2. The two models are consistent with the experimental data from CD/MCD studies and illustrate that changes in metal-coordinating residues can propagate throughout the active site.

This study investigates the absorption spectrum and rR data of the peroxo intermediate of R2-W48F/D84E. The geometric and electronic structure of this intermediate is determined via analysis of these data (normal coordinate analysis (NCA) of frequencies and time dependent Heller simulations of rR

(19) Krebs, C.; Chen, S.; Baldwin, J.; Ley, B.; Patel, U.; Edmondson, D.; Huynh, B.; Bollinger, J. *J. Am. Chem. Soc.* **2000**, *122*, 12207−12219.
(20) Riggs-Gelasco, P. J.; Shu, L. J.; Chen, S. X.; Burdi, D.; Huynh, B. H.; Que, L.; Stubbe, J. *J. Am. Chem. Soc.* **1998**, *120*, 849−860.
(21) Mitic, N.; Saleh, L.; Schenk, G.; Bollinger, J. M.; Solomon, E. I. *J. Am. Chem. Soc.* **2003**, *125*, 11200−11201.
(22) Burdi, D.; Willems, J. P.; Riggs-Gelasco, P.; Antholine, W. E.; Stubbe, J.; Hoffman, B. M. *J. Am. Chem. Soc.* **1998**, *120*, 12910−12919.
(23) Lee, S.; Lipscomb, J. *Biochemistry* **1999**, *38*, 4423−4432.
(24) Valentine, A.; Stahl, S.; Lippard, S. *J. Am. Chem. Soc.* **1999**, *121*, 3876−3887.
(25) Liu, K.; Valentine, A.; Wang, D.; Huyhn, B.; Edmonson, D.; Salifoglou, A.; Lippard, S. *J. Am. Chem. Soc.* **1995**, *117*, 10174−10185.
(26) Shu, L. J.; Nesheim, J. C.; Kauffmann, K.; Münck, E.; Lipscomb, J. D.; Que, L. *Science* **1997**, *275*, 515−518.
(27) Gherman, B. F.; Baik, M.-H.; Lippard, S. J.; Friesner, R. A. *J. Am. Chem. Soc.* **2004**, *126*, 2978−2990.
(28) Siegbahn, P. E. M. *Inorg. Chem.* **1999**, *38*, 2880−2889.
(29) Broadwater, J. A.; Ai, J. Y.; Loehr, T. M.; Sanders-Loehr, J.; Fox, B. G. *Biochemistry* **1998**, *37*, 14664−14671.
(30) Broadwater, J. A.; Achim, C.; Münck, E.; Fox, B. G. *Biochemistry* **1999**, *38*, 12197−12204.
(31) Lyle, K.; Moenne-Loccoz, P.; Ai, J.; Sanders-Loehr, J.; Loehr, T.; Fox, B. *Biochemistry* **2000**, *39*, 10507−10513.
(32) Brunold, T. C.; Tamura, N.; Kitajima, N.; Morooka, Y.; Solomon, E. I. *J. Am. Chem. Soc.* **1998**, *120*, 5674−5690.
(33) Baldwin, J.; Voegtli, W.; Khidekel, N.; Moenne-Loccoz, P.; Krebs, C.; Pereira, A.; Ley, B.; Huynh, B.; Loehr, T.; Riggs-Gelasco, P.; Rosenzweig, A.; Bollinger, J. *J. Am. Chem. Soc.* **2001**, *123*, 7017−7030.
(34) Krebs, C.; Bollinger, J.; Theil, E.; Huynh, B. *J. Biol. Inorg. Chem.* **2002**, *7*, 863−869.
(35) Wei, P.; Skulan, A. J.; Mitic, N.; Yang, Y. S.; Saleh, L.; Solomon, E. I.; Bollinger, J. M. *J. Am. Chem. Soc.* **2004**, in press.
(36) Dunietz, B. D.; Beachy, M. D.; Cao, Y. X.; Whittington, D. A.; Lippard, S. J.; Friesner, R. A. *J. Am. Chem. Soc.* **2000**, *122*, 2828−2839.

Chart 1. Spectroscopically calibrated DFT optimized structures of the biferrous site of (a) R2-W48F/D84E and (b) R2-wt. (ref 35)[a]

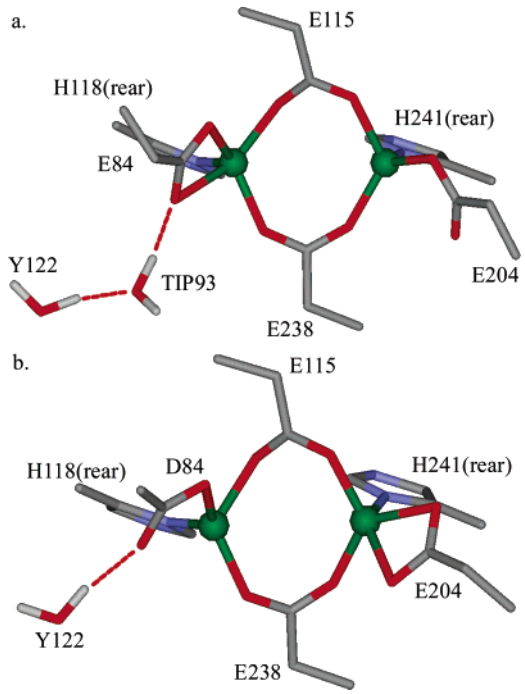

[a] Hydrogens and hydrogen-bonding elements of the model are omitted for clarity. Y122 is modeled by H_2O in each case, and "TIP93" is a water molecule. Hydrogen bonds are indicated by dashed lines.

excitation profiles and absorption data), comparison to previously studied model complexes, and geometries obtained from DFT geometry optimizations of large models (95 atoms) of the R2-W48F/D84E active site. DFT is used to explore the relative energies of various peroxo intermediate structures within the constraints of the protein pockets of both R2-W48F/D84E and R2-wt. These results are discussed in relation to other biological biferric peroxo intermediates.

2. Experimental Section

2.1. Protein Samples. Introduction of the W48F substitution into the *Eschericia coli nrdB* gene that encodes the R2 protein was accomplished as previously described.[14] The D84E mutation was introduced separately, following the procedure outlined in ref 18.

To prepare samples of the R2-W48F/D84E peroxo intermediate suitable for rR studies, an O_2 saturated solution of apo-protein ~2 mM in concentration (in 100 mM Hepes buffer, pH 7.6) was mixed at 5 ± 2 °C in a rapid-flow unit with an equal volume of an O_2 saturated solution containing 4 equiv of Fe^{2+} relative to apo-R2 (in 0.005 N H_2SO_4). The reaction mixture was guided into an open-ended glass capillary tube (1 mm × 4 cm) that was immersed in cold isopentane (123 K) ~1 s after filling to obtain frozen samples exhibiting the greenish-blue color characteristic of the R2-W48F/D84E peroxo intermediate.

2.2. Spectroscopy. Absorption data of the R2-W48F/D84E variant were obtained at 5 ± 2 °C using a HP8453 diode array spectrophotometer. Raman spectra were recorded upon excitation with Kr^+ (Coherent I90C−K) and Ar^+ (Coherent Sabre 25/7) ion lasers with incident power in the 20−30 mW range using an ~135° backscattering arrangement. The glass capillary tubes containing the frozen protein intermediate were immersed in a liquid-N_2-filled EPR quartz dewar (Wilmad glass) at 77 K. The scattered light was dispersed by a triple monochromator (Spex 1877 CP, equipped with 1200, 1800, and 2400 grooves/mm gratings) and detected with a back-illuminated CCD camera (Princeton Instruments ST-135). Raman intensities were quantified relative to the ice scattering peak at 228 cm^{-1}. Each data point included in the rR excitation profiles presented represents the average of at least 5 independent measurements on three different samples. Each of these independent measurements varies by less than 5% from the reported mean values.

2.3. Computational. Density functional theory (DFT) calculations were carried out on an SGI 2000 computer using the Jaguar 4.1 package for geometry optimizations of the models described below. All calculations were spin-unrestricted (SU), broken symmetry (BS), allowing for an accurate description of the electronic structure of antiferromagnetically coupled systems. Preliminary calculations were performed on a model of the crystallographically[37] and spectroscopically[32] characterized *cis* μ-1,2 peroxo $[Fe^{III}]_2$ model complex, $[Fe^{III}_2(O_2)(OBz)_2\{HB(pz')_3\}_2]$. A truncated computational model of this species, $[Fe_2O_2(O_2CH)_2(NH_3)_6]^{2+}$, was used to compare to previous DFT descriptions.[32] The model was geometry optimized using both the BP86 and B3LYP density functionals with an LACVP* basis set. The BP86 calculation reproduced a biferric peroxo species, while B3LYP predicted a weakly bound $Fe^{II}Fe^{II}$−dioxygen complex, inconsistent with experiment (vide infra). This suggested that the BP86 functional is better suited for investigation of biferric peroxo species and, hence, was selected for this study. Geometry optimizations were performed on models of the R2 active site derived from the crystal structures of R2-W48F/D84E and R2-wt protein, respectively. Optimizations utilized the default geometry optimization criteria of Jaguar 4.1.[38] The R2 active site model includes the six coordinating residues (D/E84, E115, H118, E204, E238, H241) truncated at the α-carbon position[39] and analogues of the principle residues involved in hydrogen-bonding to the coordinating residues (Q43, Q87, W111, S114, Y122, D237)[40] as described previously for a study of the biferrous state of R2-W48F/D84E and wt.[35] This resulted in a model consisting of 93 (R2-W48F/D84E) and 87 (R2-wt) atoms (representative views of the W48F/D84E model are included in the Supporting Information).[41] The H-bonding residues included correlate well with those identified as having strong interactions with the six iron-coordinating residues from combined QM/MM calculations.[12] For geometry optimizations, the iron atoms were described by the LACVP* double-ζ basis set,[42] atoms within three bonds of the iron atoms used 6-31G*, and all others used 6-31G. The basis set size was increased to triple-ζ for determining energies, using the LACV3P* basis set. Electronic structure descriptions were obtained using the Amsterdam Density Functional (ADF) 2000 software package developed by Baerends et al..[43,44] ADF calculations were performed with an integration constant of 4.0 and the Vosko−Wilk−Nusair local

(37) Kim, K.; Lippard, S. *J. Am. Chem. Soc.* **1996**, *118*, 4914−4915.
(38) Geometry convergence criteria were as follows: change in total energy, ΔE < 5e-5 Hartrees, maximum local energy gradient, $\delta E/\delta S$ < 4.5e-4 Hartrees/Å, $\delta E/\delta S$(RMS) < 3e-4 Hartrees/Å, ΔS < 1.8e-3 Å, ΔS(RMS) < 1.2e-5 Å. Frequency calculations to verify that true minima had been attained were not possible as Jaguar 4.1 and subsequent Jaguar 5.0 have not implemented parallelized analytical frequency determination. Such calculations will be performed once this functionality has been added.
(39) The residue truncation was performed as follows; the α-carbon was replaced by a hydrogen atom with concommitent shortening of the α-C−β-C bond to 1.08 Å, with the β-C retaining its original position. This hydrogen was then frozen in all geometry optimizations.
(40) The hydrogen bonding residues were truncated to the smallest reasonable models providing similar hydrogen bonding interactions as observed in the protein. These were as follows: Q43; formamide, $COHNH_2$, Q87; ammonia, NH_3, W111; ammonia, NH_3, S114; water, H_2O, Y122; water, H_2O, D237; formate, CHO_2^-. The positions of the heavy atoms (C, N, O) were frozen along with the positions of hydrogens replacing carbon atoms. Q43 and Q87 were modeled differently (as formamide and ammonia, respectively) as the R-group nitrogen of Q43 was located 2.8 Å from a carboxylate oxygen on D237 suggesting hydrogen bonding between these two residues which may have been of importance to the geometry of the active site. W/F48 residue, the second mutation from wt, was not included in the model as it does not coordinate to either iron or iron-coordinated residues.
(41) The atom count differs between the two calculations due to the addition of a methylene ($-CH_2-$) by the D84E mutation and the introduction of a water molecule which is coordinated to E84 in the mutant.
(42) Hay, P.; Wadt, W. *J. Chem. Phys.* **1985**, *82*, 299−310.
(43) Baerends, E. J.; Ellis, D. E.; Ros, P. *J. Chem. Phys.* **1973**, *2*, 42.
(44) te Velde, G.; Barerends, E. J. *Int. J. Comput. Phys.* **1992**, *99*, 84.

density approximation[45] in conjunction with the nonlocal gradient corrections of Becke and Perdew.[46,47] A triple-ζ Slater-type orbital basis set with a single polarization function (ADF basis set IV) was used for each atom. Core orbitals were frozen through 1s (C, N, and O) and 2p (Fe). The ADF calculations were performed on a truncated (64 atom) version of the geometry optimized model, removing hydrogen-bonding residues more than two bonds separated from the diiron center (Q43 and D237) and replacing propanoate groups with acetate and 2-methylimidazole with imidazole to improve the speed of calculations. Orbital occupation tables were generated using AOMIX.[48,49] Complete coordinates of all the geometry optimized models discussed in the text are included in Supporting Information.

2.4. Normal Coordinate Analyses. Normal coordinate analyses (NCAs) of the vibrational data of the R2-W48F/D84E peroxo intermediate were performed on the Fe_2O_2 cores of the three hypothetical active-site models generated using Jaguar 4.1 geometry optimizations. The analyses were based on the Wilson FG matrix method using a Urey−Bradley force field, as implemented in a modified version of the Schachtschneider program.[50,51] All input coordinates used in the NCAs are included in the Supporting Information.

2.5. Excited-State Analysis. Simultaneous fits of the absorption and rR excitation profile data of the R2-W48F/D84E peroxo intermediate were performed using the time-dependent theory of electronic spectroscopy implemented in a script for Mathcad PLUS 6.0. A direct modeling approach was used to search for the set of excited-state parameters that produce the best simultaneous fit of the absorption and rR profile data. [52]

3. Results and Analysis

3.1. Spectroscopy. Electronic absorption and rR data were collected for the peroxo-R2-W48F/D84E species and analyzed within the framework of the normal coordinate analysis (NCA−Raman spectrum simulation) and time-dependent Heller theory (rR profile and absorption spectrum simulation). Three peroxo-biferric coordination modes (*cis* μ-1,2-, *trans* μ-1,2- and μ-η^2:η^2-peroxo) identified by DFT geometry optimizations (vide infra) were evaluated on the basis of the experimental data to assess the core structure of the peroxo-R2-W48F/D84E species.

3.1.1. Results. The low-temperature absorption and rR data for the R2-W48F/D84E peroxo species are shown in Figure 1, top. For comparison, Figure 1 also shows spectroscopic data from two model complexes; $[Fe^{III}_2(O_2)(OBz)_2\{HB(pz')_3\}_2]$ [32] (Figure 1, middle), a crystallographically characterized[37] *cis* μ-1,2 peroxo $[Fe^{III}]_2$ model complex with each ferric ion capped by a tridentate N-donor ligand and bridged by two carboxylates (Chart 2, left), and $[Fe^{III}(EDTA)(O_2)]^{3-}$ (Figure 1 bottom), an η^2-coordinated ferric peroxo complex bound to a tetradentate EDTA ligand (Chart 2, right). Both the R2-W48F/D84E peroxo species and $[Fe^{III}_2(O_2)(OBz)_2\{HB(pz')_3\}_2]$ exhibit a prominent absorption band in the visible spectral region and the onset of more intense features in the UV. Additionally, both species display similar rR enhancement of two vibrations near 450 and

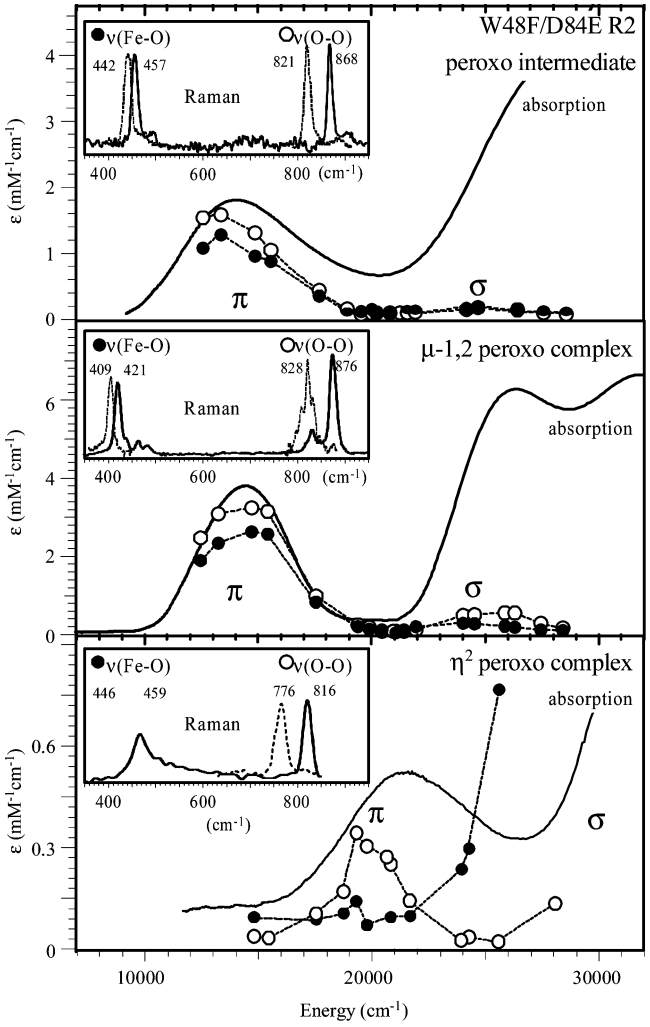

Figure 1. (Top) Absorption spectrum and rR profiles of the R2-W48F/D84E peroxo species. (Inset) ^{16}O (solid) and ^{18}O (dashed) rR spectra (647 nm excitation wavelength). (Middle) Absorption spectrum and rR profiles of $[Fe^{III}_2(O_2)(OBz)_2\{HB(pz')_3\}_2]$ from ref 32. (Inset) ^{16}O (solid) and ^{18}O (dashed) rR spectra (647 nm excitation wavelength). (Bottom) Absorption spectrum and rR profiles of $[Fe^{III}(O_2)EDTA]^{3-}$ from ref 53. (Inset) ^{16}O (solid) and ^{18}O (dashed) rR spectra (530 nm excitation wavelength). Note the differences in extinction coefficient scales for the three compounds.

Chart 2. Schematics of the Coordination Environment of the *cis* μ-1,2-Peroxo $[Fe^{III}]_2$ Dimer, $[Fe^{III}_2(O_2)(OBz)_2\{HB(pz')_3\}_2]$ (Left), and the Side-On η^2-Peroxo Fe^{III} Monomer, $[Fe^{III}(O_2)EDTA]^{3-}$, (Right)

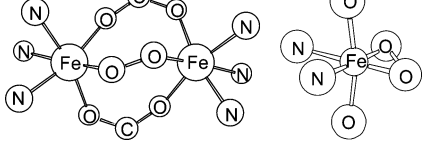

870 cm^{-1},[18] labeled ν(Fe−O) and ν(O−O) in the insets in Figure 1, upon excitation into the broad band centered at ~14 000 cm^{-1}. These vibrations have been assigned to the Fe−O and O−O stretches, respectively, on the basis of their shifts to lower frequencies upon $^{16}O\rightarrow^{18}O$ isotopic substitution. The same features are also observed for excitation in resonance with the intense near-UV absorption features, but the degree of enhancement is greatly reduced (cf. rR excitation profiles in Figure 1).

The fact that the absorption and rR excitation profile data for the R2-W48F/D84E peroxo species and the *cis* μ-1,2 peroxo $[Fe^{III}]_2$ model complex are qualitatively very similar suggests

(45) Vosko, S. H.; Wilk, L.; Nusair, M. *Can. J. Phys.* **1980**, *58*, 1200.
(46) Perdew, J. P. *J. Chem. Phys.* **1986**, *33*, 8822.
(47) Becke, A. D. *J. Chem. Phys.* **1986**, *84*, 4524.
(48) Gorelsky, S. I. *AOMix Program*, revision 5.69, http://www.obbligato.com/software/aomix/.
(49) Gorelsky, S. I.; Lever, A. B. P. *J. Organomet. Chem.* **2001**, *635*, 187−196.
(50) Schachtschneider, J. H. Technical Report No. 57-65, Shell Development Company: Emeryville, CA, 1966.
(51) Fuhrer, H.; Kartha, V. B.; Kidd, K. G.; Kreuger, P. J.; Mantsch, H. H. Computer Programs for Infrared Spectroscopy, Bulletin No. 15, National Research Council of Canada, 1976.
(52) Myers, A. B.; Mathies, R. A. In *Biological applications of Raman spectroscopy*; Spiro, T. G., Ed.; John Wiley & Sons: New York, 1987; Vol. 2.

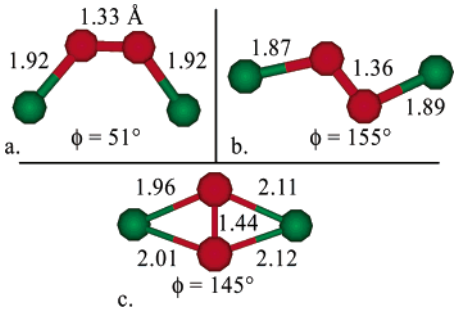

Figure 2. Geometry optimized Fe_2O_2 core models for normal coordinate analysis. (a) *cis* μ-1,2-peroxo from the R2-W48F/D84E model, (b) *trans* μ-1,2-peroxo from the R2-W48F/D84E model, and (c) μ-η^2:η^2 peroxo from the R2-wt model. Iron is shown in green, and oxygen, in red. Bond lengths are in angstroms, and ϕ is the core torsion angle.

that the two chromophoric units possess similar geometric and electronic structures. In comparison, absorption and rR data reported for the η^2-O_2^{2-} complex, $[Fe^{III}(EDTA)(O_2)]^{3-}$,[53] (Figure 1, bottom) are strikingly different: (i) rR spectra identify an O−O stretch at 816 cm^{-1}, much lower in frequency than the R2-W48F/D84E peroxo species (868 cm^{-1}), and an Fe−O stretch at 459 cm^{-1} (457 cm^{-1} in protein); (ii) the absorption spectrum exhibits a prominent feature at ~21 500 cm^{-1}, carrying about 30% of the intensity of the ~14 000 cm^{-1} band in the spectrum of the R2-W48F/D84E peroxo species, and an approximately 10× more intense feature in the near UV centered at ~30 000 cm^{-1}. rR spectra obtained upon excitation into the visible band of $[Fe^{III}(O_2)EDTA]^{3-}$ are dominated by the O−O stretch, whereas excitation in resonance with its UV feature gives rise to almost exclusive enhancement of the Fe−O stretch. Importantly, the rR enhancement of ν(Fe−O) for UV excitation greatly exceeds that of ν(O−O) for visible excitation, which is markedly different from the rR excitation profile data of the R2-W48F/D84E peroxo species and the synthetic *cis* μ-1,2 peroxo $[Fe^{III}]_2$ complex (Figure 1). Previous studies[32,53] have shown that spectral differences between the *cis* μ-1,2 peroxo $[Fe^{III}]_2$ dimer and the side-on η^2 peroxo Fe^{III} monomer are directly related to the different electronic structures associated with the different binding modes of peroxide in these two species. Thus, the striking correlation of the spectroscopic data in Figure 1 to the *cis* μ-1,2 model complex suggests that in the R2-W48F/D84E peroxo species the peroxide moiety bridges the two ferric centers in an end-on μ-1,2 binding mode.

3.1.2. Fe−O and O−O Force Constants. Previous vibrational studies observed that the modal energies of the R2-W48F/D84E peroxo intermediate are most consistent with symmetric μ-1,2 peroxo model complexes[18] while the most recent DFT geometry optimizations of peroxo models based on the R2 ligand set favor a distorted μ-η^2:η^2 peroxo structure.[54] The energies of vibrational modes are sensitive to the geometry of the species under investigation,[55] allowing these geometrically dissimilar structures to be evaluated in light of the experimental data. DFT geometry optimizations (vide infra) have identified three coordination geometries (Figure 2) with similar constituents (a peroxo ligand bridging a biferric active site) but very different geometries. They are a *cis* μ-1,2 peroxo (Figure 2a), a *trans* μ-1,2 peroxo (Figure 2b), and a μ-η^2:η^2 peroxo (Figure 2c) structure. Normal coordinate analysis (NCA) is ideally suited for differentiating such structures. [55] A Urey−Bradley force field was chosen to facilitate comparison with the results from an NCA performed on the *cis* μ-1,2 peroxo $[Fe^{III}]_2$ model complex, $[Fe^{III}_2(O_2)(OBz)_2\{HB(pz')_3\}_2]$.[32]

In the *cis* and *trans* μ-1,2 peroxo complexes, the two Fe−O bonds are of equal length (Figure 2), permitting the Fe−O stretches to be modeled by a single force constant in the NCA (Table 1). In each model, the Fe−O−O bending force constant was fixed at 0.3 mdyne/Å, consistent with published values for end-on μ-1,2 peroxo $[Fe^{III}]_2$ dimers,[32] while a suitable Urey−Bradly nonbonded interaction constant (k_{UB}) was also included for the bending modes. The μ-η^2:η^2 peroxo core has significantly different Fe−O bond lengths (Figure 2c), requiring three different force constants to be used for the 1.96 Å, 2.01 Å, and 2.11/2.12 Å Fe−O bonds, with shorter bond lengths correlating with a larger stretching force constant (Badger's rule[56,57]). k_{Fe-O-O} and k_{UB} are not included in the μ-η^2:η^2 and η^2 Fe^{III} model complex NCAs, as these geometries allow the vibrational modes to be modeled most easily in terms of stretching motions along the O−O and Fe−O bonds. These force constants were then fitted to the experimental frequencies of ν(Fe−O) and ν(O−O) obtained for the ^{16}O and ^{18}O isotopomers.

The results of this analysis are summarized in Table 1 along with the previously published NCA parameters of $[Fe^{III}_2(O_2)(OBz)_2\{HB(pz')_3\}_2]$ and $[Fe^{III}(EDTA)(O_2)]^{3-}$ for comparison. The *cis* μ-1,2 R2 peroxo model fits the experimental data using Fe−O and O−O stretching force constants consistent with those previously determined for $[Fe^{III}_2(O_2)(OBz)_2\{HB(pz')_3\}_2]$. In contrast, the Fe−O stretching force constant for the *trans* μ-1,2 peroxo (k_{Fe-O} = 1.11 mdyne/Å) and μ-η^2:η^2 peroxo ($k_{Fe-O} \approx$ 3.72 mdyne/Å) structures are inconsistent with the values previously reported for ferric iron−peroxo complexes. No *trans* μ-1,2 biferric−peroxo complexes have been previously identified in the literature, but k_{Fe-O} for such a molecule would be expected to be similar to that observed in end-on bridged *cis* μ-1,2 complexes; k_{Fe-O} = 1.99 mdyne/Å for $[Fe^{III}_2(O_2)(OBz)_2\{HB(pz')_3\}_2]$. However, this is 80% greater than that required by the *trans* μ-1,2 peroxo structure of Figure 2c with $\nu_{sym(Fe-O)}$ = 457 cm^{-1}. A biferric μ-η^2:η^2 peroxo structure would be expected to have an Fe−O stretching force constant lower than that of the η^2 side-on monomer (k_{Fe-O} = 1.55 mdyne/Å) as the peroxo charge donation per metal would be lower in the dimer due to the peroxo ligand now being shared between two ferric ions, weakening individual Fe−O bonds. However, with $\nu_{sym(Fe-O)}$ = 457 cm^{-1}, the average calculated force constant for the μ-η^2:η^2 structure is $k_{Fe-O} \approx$ 3.72 mdyne/Å. This analysis indicates that only the *cis* μ-1,2 peroxo model of R2-W48F/D84E yields reasonable Fe−O and O−O force constants, while the *trans* μ-1,2 and μ-η^2:η^2 geometries give NCA results inconsistent with the experimental data.

The Fe−O and O−O stretching force constants for the *cis* μ-1,2 R2 peroxo structure, 2.08 and 3.09 mdyne/Å, respectively, are similar to those calculated for the $[Fe^{III}_2(O_2)(OBz)_2\{HB(pz')_3\}_2]$ model complex, 1.99 and 3.07 mdyne/Å. This small difference in stretching force constants does not cause the striking 36 cm^{-1} difference in the frequency of the symmetric Fe−O stretch (457 vs 421 cm^{-1}) between the protein intermedi-

(53) Neese, F.; Solomon, E. *J. Am. Chem. Soc.* **1998**, *120*, 12829−12848.
(54) Siegbahn, P. *Chem. Phys. Lett.* **2002**, *351*, 311−318.
(55) Wilson, E. B. J.; Decius, J. C.; Cross, P. C. *Molecular Vibrations*; Dover Publications: New York, 1980.
(56) Badger, R. M. *J. Chem. Phys.* **1934**, *2*, 128−131.
(57) Herschbach, D. R.; Laurie, V. W. *J. Chem. Phys.* **1961**, *35*, 458−463.

Table 1. Results from NCAs of the Vibrational Data of the R2-W48F/D84E Peroxo Intermediate, Obtained Using the Fe_2O_2 Core Structures of the Three Active Site Models in Figure 2, and the Experimental Frequencies and NCA Results of the $[Fe^{III}_2(O_2)(OBz)_2\{HB(pz')_3\}_2]$ and $[Fe^{III}((EDTA)(O_2)]^{3-}$ Model Complexes (Force Constants in mdyne/Å, and Frequencies in cm^{-1})

	experimental		R2 *cis* μ-1,2		R2 *trans* μ-1,2		R2 μ-η^2:η^2		experimental *cis* μ-1,2 Fe^{III}_2 model		experimental η^2 Fe^{III} model	
normal mode	$^{16}O_2$	$^{18}O_2$	$^{16}O_2$	$^{18}O_2$	$^{16}O_2$	$^{18}O_2$	$^{16}O_2$	$^{18}O_2$	$^{16}O_2$	$^{18}O_2$	$^{16}O_2$	$^{18}O_2$
ν(O−O)	868	821	870	821	869	819	867	822	876	828	816	776
ν_{as}(Fe−O)			567	540	398	381	910	870				
ν_{sym} (Fe−O)	457	442	458	439	461	437	455	447	421	409	459	446
δ_{as} (Fe−O−O)			275	262	160	156	805	761				
δ (Fe−O−O)			142	136	134	130	429	408				
					Force Constant							
k_{O-O}			3.09		3.42		2.89		3.07		3.02	
k_{Fe-O}			2.08		1.11		3.92[a]		1.99		1.55	
							3.74[b]					
							3.51[c]					
k_{Fe-O-O}			0.30		0.30				0.30			
k_{UB}			0.10		0.10				0.1			

[a] k_{Fe-O} for the r(Fe−O) = 1.96 Å bond (Figure 2c). [b] k_{Fe-O} for the r(Fe−O) = 2.05 Å bond. [c] k_{Fe-O} for the r(Fe−O) = 2.11 and r(Fe−O) = 2.12 Å bonds.

ate and the model. Rather, this difference in frequency arises from different bond angles in the two models which result in different degrees of mechanical coupling between the Fe−O and O−O stretching motions. The Fe−O−O angles are 125° and 121° in the DFT-optimized *cis* μ-1,2 R2 peroxo structure and 129° in the crystallographically characterized *cis* μ-1,2 model complex. Previous NCA simulations on biferric *cis* μ-1,2 peroxo structures have shown that such a difference in geometry would result in the symmetric Fe−O stretch changing by ∼30 cm^{-1},[32] accounting for the observed difference in the frequency of the symmetric Fe−O stretch.

A recent study has assigned a short Fe−Fe separation of 2.5 Å to the EXAFS data from the R2-W48A/D84E peroxo intermediate.[58] This species is proposed to be analogous to the R2-W48F/D84E peroxo−biferric species analyzed above. To test this proposed geometric constraint against the available vibrational data, NCA simulations were performed. These used a symmetric *cis* μ-1,2 peroxo coordination geometry with r(Fe−O) = 1.88 Å and r(O−O) = 1.40 Å, consistent with the $[Fe^{III}_2(O_2)(OBz)_2\{HB(pz')_3\}_2]$ crystal structure,[37] and varied the Fe−O−O−Fe torsion angle through the full range of possible values from 0° (planar) to 91.5° (a butterfly μ-η^2:η^2 structure). This range varied the Fe−O−O angle from 107° (planar) down to 68° (butterfly). The results (Supporting Information) found that the O−O stretching force constant, k_{O-O}, ranged from 3.48 to 3.23 mdyne/Å along the progression from planar to butterfly structures and that k_{Fe-O} varied from ∼1.63 mdyne/Å at the planar/butterfly extrema to 1.51 mdyne/Å at a 45° torsion angle. This requires that k_{Fe-O} be 20−25% smaller and k_{O-O} be 5−13% larger in the double variant peroxo than in the *cis* μ-1,2 model complex. This result is inconsistent with the decrease in peroxo donation identified by the decreased intensity of the ∼14 000 cm^{-1} charge-transfer transition in the protein intermediate relative to the model complex (see section 3.1.3). Electron density in the peroxide π^*_π donor orbital weakens the O−O bond due to the antibonding nature of this orbital. Thus, lowering the donation from π^*_π would result in a weaker O−O bond in the protein peroxo intermediate relative to the model complex, opposite that predicted by the vibrational data. Thus, our analysis does not support a short (2.5 Å) Fe−Fe distance in the R2-W48F/D84E peroxo−biferric species.

3.1.3. Peroxide→Fe Charge Donation. A crucial property of the peroxo $[Fe^{III}]_2$ intermediates of non-heme iron enzymes is charge distribution, as this determines the strength of metal−ligand interactions and the activation of the Fe_2O_2 unit toward transformation to subsequent high-valent Fe-oxo species. The donor strength of a given ligand can be estimated from the sum of the integrated absorption intensities of all CT transitions associated with this ligand. While absorption band overlaps in the near-UV spectral region complicate quantification of the total donor strength of the peroxide ligand in μ-1,2 peroxo $[Fe^{III}]_2$ dimers, the π-charge donation from the peroxide π^*_π donor orbital[59] into the Fe $3d_\pi$ acceptor orbitals, $C_{\pi^*_\pi \rightarrow 3d_\pi}$ (corresponding to the square of the orbital mixing coefficient), can be estimated from the intensity of the prominent peroxide-to-Fe CT absorption feature in the visible region (Figure 1):

$$C_{\pi^*_\pi \rightarrow 3d_\pi} = \kappa \frac{f}{\nu_{max}|\mathbf{r}|^2} \qquad (1)$$

κ is a constant (9.22×10^{-2} Å), f and ν_{max} are the oscillator strength[60] and transition energy of the CT transition under investigation, and **r** is the transition vector, which is assumed to coincide with the peroxide−Fe bond vector. While the calculated value of $C_{n^*_\pi \rightarrow 3d_\pi}$ is not a quantitative measure of bond covalency, it permits a useful comparison between similar complexes.

The values of f and ν_{max} for the protein peroxo intermediate and $[Fe^{III}_2(O_2)(OBz)_2\{HB(pz')_3\}_2]$ were determined from the Gaussian-fit area and peak energy (Figure 3, Table 2) of the ∼14 000 cm^{-1} feature in their absorption spectra (Figure 1, top and middle panels). The transition vector length, **r**, is the length of the Fe−O bond. This analysis reveals that the π-donor strength of the peroxide in the R2-W48F/D84E protein relative to the *cis* μ-1,2 peroxo $[Fe^{III}]_2$ model complex is reduced by 44% (±7%).[61] In contrast with the sharp Gaussian band shape

(58) Baldwin, J.; Krebs, C.; Saleh, L.; Stelling, M.; Huynh, B.; Bollinger, J.; Riggs-Gelasco, P. *Biochemistry* **2003**, *42*, 13269−13279.

(59) A π* orbital of the peroxo unit, O_2^{2-}, is labeled π^*_σ if it has σ-overlap with the metal and π^*_π for π-overlap with the metal.

(60) Hitchman, M. A.; Riley, M. J. In *Inorganic Electronic Structure and Spectroscopy*; Solomon, E. I., Lever, A. B. P., Eds.; John Wiley & Sons: New York, 1999; Vol. 2.

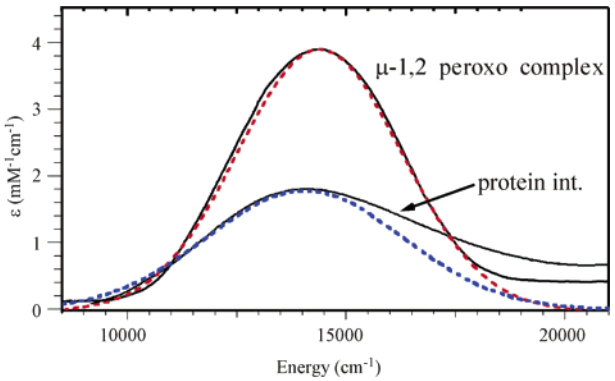

Figure 3. Gaussian fit to the ~14 000 cm^{-1} feature in the R2-W48F/D84E peroxo intermediate and the μ-1,2-peroxo complex, $[Fe^{III}_2(O_2)(OBz)_2\{HB(pz')_3\}_2]$.

Table 2. Gaussian Fit Data for the ~14 000 cm^{-1} Band of the R2-W48F/D84E Peroxo Intermediate and the μ-1,2-Peroxo Complex, $[Fe^{III}_2(O_2)(OBz)_2\{HB(pz')_3\}_2]$

	ν_{max} (cm^{-1})	f ($\times 10^{-2}$)	r (Å)	C_{prot}/C_{model}
R2-W48F/D84E protein int.	14 150	4.11	1.92[a]	0.56
μ-1,2-peroxo complex	14 400	7.20	1.88	

[a] Average Fe−O bond distance of the DFT-calculated R2-W48F/D84E μ-1,2-peroxo model.

at 14 400 cm^{-1} for the model complex, the absorption feature at 14 100 cm^{-1} for the protein intermediate tails away to higher energy. This behavior commonly occurs due to intensity sharing with weaker transitions at similar energy, leading to a smeared out absorption envelope. If this mechanism is invoked for the protein intermediate and the oscillator strength is instead taken to be the integrated intensity of the absorption spectrum over the 8000−20 000 cm^{-1} interval, the relative donor strength is 70% (±11%), a value that represents an upper limit for the relative peroxo donation. As a similar reduction occurs for the σ-donor strengths (see section 3.1.4), the total peroxide → Fe charge donation is reduced in the protein intermediate, indicating that the charge on the ferric iron is decreased in the protein due to the presence of additional anionic ligands (i.e., terminal carboxylate).[62] The mechanistic implications of this result with respect to the enzymatic conversion of peroxo intermediates to high-valent Fe-oxo species will be discussed.

3.1.4. Excited-State Analysis. The nature of excited state distortions associated with electronic transitions can be extracted from absorption and rR excitation profile data through application of time-dependent Heller Theory. Figure 4 shows the simulated absorption and rR excitation profile data obtained with the fitted excited-state parameters listed in Table 3. While the correspondence between the experimental and simulated absorption spectra is relatively poor, the experimental rR excitation profiles are very well reproduced by the simulation. This result suggests that additional transitions contribute to the absorption spectrum between 15 000 and 20 000 cm^{-1}, presumably Laporté

(61) The uncertainty in the percentage peroxo donation decrease is due to uncertainty in the extinction coefficient of the protein peroxo intermediate. This is due to the difficulty of calculating the proportion of a short-lived intermediate accumulated at any moment during a stopped flow experiment.

(62) This may appear inconsistent with the protein and model having similar k_{O-O} and k_{Fe-O} values (Table 1). However, a 5° change in the Fe(2)−O−O bond angle (within anticipated error of the geometry optimized model) changes the stretching force constants required to fit the experimental data by ~0.1 mdyne/Å.

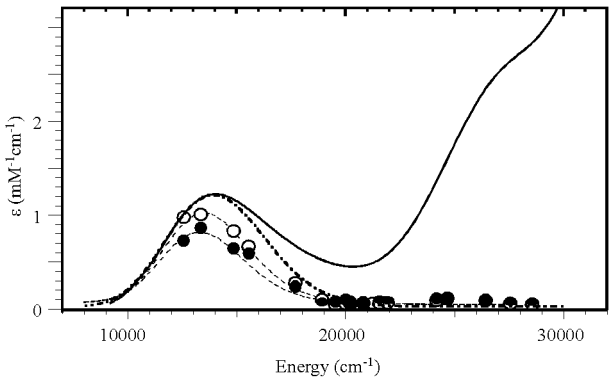

Figure 4. Comparison of the absorption spectrum (solid line) and rR profiles of the 868 cm^{-1} (○) and 457 cm^{-1} (●) modes of the R2-W48F/D84E peroxo species (solid line) with simulated absorption (dash−dotted line) and rR excitation profiles (dashed lines) obtained using the fitted excited-state parameters listed in Table 3.

Table 3. Excited-State Parameters from Simultaneous Fits of the Absorption and rR Excitation Profile Data of the R2-W48F/D84E Peroxo Intermediate and the Synthetic *cis* μ-1,2 Peroxo $[Fe^{III}]_2$ Dimer (the Same Signs of the Δ's Were Used as in Ref 32)

	R2-W48F/D84E	$[Fe^{III}]_2$ *cis* μ-1,2-Peroxo
E_0, cm^{-1}	8500	10 000
Δ(Fe−O)	3.75	3.68
Δ(O−O)	−2.25	−1.98

Table 4. Normal Mode Descriptions for the *cis* μ-1,2 Fe_2O_2 Model of Figure 2a

normal mode	eigenvectors[a,b]			potential energy distribution[b]		
	$O–O_{str}$	$Fe–O_{str}$	$Fe–O–O_{bend}$	$O–O_{str}$	$Fe–O_{str}$	$Fe–O–O_{bend}$
ν(O−O)	0.35	−0.13	−0.06	83	16	1
ν_{sym}(Fe−O)	0.07	0.15	−0.10	12	80	5

[a] Mass weighted eigenvectors, $\mathbf{L}_n$. [b] Average values: the model is not strictly of C_2 symmetry. However, this asymmetry leads to the eigenvectors and potential energy distributions differing by <5% from the average value reported in the table.

forbidden d−d transitions that acquire their intensity through spin−orbit mixing with nearby CT excited states.

To test the relative π vs σ peroxo donor strengths in the R2-W48F/D84E peroxo intermediate, an analysis of the excited-state distortions associated with the peroxide-to-Fe CT transition in the visible region was performed for the protein species and compared to the results of a similar analysis reported for the synthetic μ-1,2 model complex. The nuclear distortions of the Fe_2O_2 unit can be estimated using the following relationship between internal coordinate changes, Δr_i, and dimensionless normal coordinate displacements, Δ_n:

$$\Delta r_i = 5.8065 \sum_n \mathbf{L}_{i,n} \frac{\Delta_n}{\sqrt{\nu_n}} \qquad (2)$$

where $L_{i,n}$ is the ith element of the mass-weighted eigenvector $\mathbf{L}_n$ for the nth normal mode. Using the eigenvectors from the NCA on the *cis* μ-1,2 peroxo $[Fe^{III}]_2$ protein model (Table 4) and the Δ_n values determined from simultaneous fits to the absorption and rR data of the R2-W48F/D84E peroxo intermediate (Table 3), the distortions depicted in Chart 3 are obtained. This analysis reveals that the major distortion occurs along the Fe−O coordinates, whereas the O−O bond length change is relatively small. The large increase in Fe−O bond length by

Chart 3. Experimental Excited-State Distortion of the Fe_2O_2 Core in the R2-W48F/D84E Peroxo Intermediate Associated with the Peroxide-to-Fe CT Transition at 13 900 cm^{-1} (Figure 1)

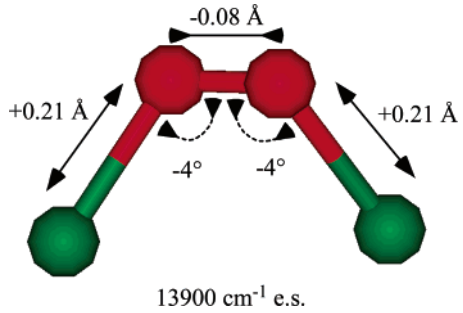

+0.21 Å demonstrates that a dominant Fe-peroxide bonding interaction has been disrupted in the corresponding excited state. Virtually identical results were obtained for the *cis* μ-1,2 peroxo $[Fe^{III}]_2$ model complex (Δr(Fe−O) = 0.20 Å, Δr(O−O) = 0.06 Å, $\Delta\theta$(Fe−O−O) = 5°) where the large increase in Fe−O bond length was attributed to an almost complete elimination of the Fe−peroxide π-bond. Thus, in both cases the relative σ-contribution to the Fe−peroxide bonding interaction must be similar and less important than the π-contribution; otherwise the distortions along the Fe−O coordinates would be considerably smaller.

3.2. Computational. 3.2.1. Density Functional Selection: The *cis* μ-1,2 Biferric Peroxo Model Complex. The density functional used in this study (BP86) was chosen based upon correlation with the geometric and electronic structure of the previously studied μ-1,2 biferric peroxo model complex, $[Fe^{III}_2(O_2)(OBz)_2\{HB(pz')_3\}_2]$. The same computational model used in previously published ADF DFT calculations,[32] $[Fe_2O_2(O_2CH)_2(NH_3)_6]^{2+}$, was geometry optimized in Jaguar 4.1 using the LACVP* basis set and the BP86 and B3LYP density functionals (Chart 4). The geometry optimized cores obtained from the two functionals are shown in Figure 4, and the energies and compositions of the Fe1 3d-based unoccupied molecular orbitals (MOs) are shown in Tables 5 and 6.

The orbital compositions given in Tables 5 and 6 show that the BP86 functional predicts a biferric−peroxo complex (five singly occupied Fe 3d-orbitals on each metal), while B3LYP predicts a weakly bound biferrous−dioxygen complex (one occupied minority-spin Fe d-based orbital, the HOMO (*xy*), on both Fe1 and Fe2). The BP86 calculation is consistent with the

Chart 4. Geometry Optimized Cores of an $[Fe_2O_2(HCO_2)_2(NH_3)_6]^{2+}$ Model Using BP86 (Left) and B3LYP (Right) Density Functionals

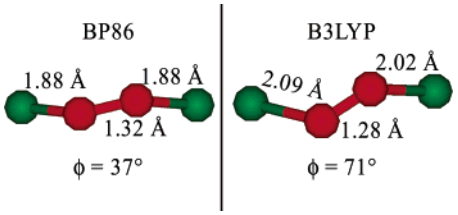

electronic nature of the $[Fe^{III}_2(O_2)(OBz)_2\{HB(pz')_3\}_2]$ model complex, while B3LYP has a markedly different geometric and electronic description of this complex, indicating that BP86 is a more suitable functional than B3LYP for this study. This calibration has led to the use of the BP86 density functional in DFT geometry optimization of hypothetical active-site models of the R2-W48F/D84E peroxo intermediate.

Table 5. Energies (eV) and Compositions of Relevant MOs from an SU-BS Calculation on $[Fe_2O_2(HCO_2)_2(NH_3)_6]^{2+}$ Using the BP86 Functional, Jaguar 4.1, and the LACV3P* Basis Set[63]

							peroxo		
E (eV)		orb[a]	N′, O′	Fe1	O3	O4	orb	Fe2	N′, O′
−9.21		z^2	15	71	9	4	π^*_σ	1	0
−9.76		*xy*	23	75	0	0		0	2
−10.82		*yz*	2	64	21	11	π^*_π	2	1
−10.98		x^2-y^2	4	87	5	3	π^*_π	1	1
−11.12	LUMO	*xz*	3	82	5	4	π^*_σ	2	4
total peroxo character in Fe 3d-based MOs			40 + 22				= 62%		

[a] Coordinate system: z = Fe−O_{peroxo} bond vector, $x \approx$ Fe−$O_{carboxylate\ 1}$ bond vector, $y \approx$ Fe−$O_{carboxylate\ 2}$ bond vector.

Table 6. Energies (eV) and Compositions of Relevant MOs from an SU-BS Calculation on $[Fe_2O_2(HCO_2)_2(NH_3)_6]^{2+}$ Using the B3LYP Functional, Jaguar 4.1, and the LACV3P* Basis Set

							peroxo		
E (eV)		orb[a]	N′, O′	Fe1	O3	O4	orb	Fe2	N′, O′
−6.71		x^2-y^2	11	85	2	1		0	0
−7.54		z^2	14	81	1	0		0	3
−8.52		*yz*	4	94	0	0		0	2
−8.58		*xz*	3	93	1	1		0	3
−10.25	LUMO	*xy*	1	22	43	29	π^*_π	3	2
−12.53	HOMO	*xy*	5	73	6	11	π^*_π	3	3
total peroxo character in Fe 3d-based MOs			10 + 13				= 3%		

[a] Coordinate system: x = Fe−O_{peroxo} bond vector, $y \approx$ Fe−$O_{carboxylate\ 1}$ bond vector, $z \approx$ Fe−$O_{carboxylate\ 2}$ bond vector.

Table 7. Compositions of the Fe1 3d-Derived Unoccupied MOs from an SU-BS Calculation for the $[Fe_2O_2(HCO_2)_2(NH_3)_6]^{2+}$ Model of $[Fe^{III}_2(O_2)(OBz)_2\{HB(pz')_3\}_2]$ Calculated Using the ADF Package[a 63]

							peroxo		
E (eV)		orb	N′, O′	Fe1	O3	O4	orb	Fe2	N′, O′
−8.834		z^2	9	70	8	4	π^*_σ	0	0
−9.308		*xy*	15	74	0	0		0	0
−10.312		*yz*	0	60	22	12	π^*_π	2	0
−10.606		x^2-y^2	1	85	4	1		0	0
−10.729	LUMO	*xz*	1	78	7	4	π^*_π	3	0
total peroxo character in Fe 3d-based MOs			41 + 21				= 62%		

[a] The orbital contributions in this table differ slightly from those in Table 5 as the basis sets used are different (Jaguar calculations were performed using LACV3P*, and ADF calculations used ADF Basis Set IV).

The most notable difference between the geometry of the BP86 optimized structure (Figure 4a) and the crystal structure is that the calculated O−O bond length (1.32 Å) is shorter than that in the crystal structure (1.40 Å). Superficial analysis of such a bond length would suggest that the oxygen ligand is a superoxide. However, analysis of the calculated MO description reveals five unoccupied minority-spin d-orbitals on each iron and no unoccupied $O_2(\pi^*)$, indicating that the electronic structure of the BP86 optimized $[Fe_2O_2(HCO_2)_2(NH_3)_6]^{2+}$ model is that of a biferric peroxo. These results suggest that the double-ζ LACVP* basis set underestimates the O−O bond length in biferric peroxo complexes, an observation that will need to be recalled during the remainder of this study. The d-orbital occupations for an ADF calculation on the $[Fe_2O_2(HCO_2)_2(NH_3)_6]^{2+}$ model using the coordinates from the Jaguar BP86 geometry optimization are given in Table 7 and will be used to correlate differences between the spectra of the

Table 8. Key Structural Features and Total Energies of the DFT Geometry Optimized Active Site Models of the R2-wt and R2-W48F/D84E Peroxo Intermediate

	R2-W48F/D84E		R2-wt	
	cis μ-1,2 $[Fe^{III}]_2$	*trans* μ-1,2 $[Fe^{III}]_2$	*cis* μ-1,2 $[Fe^{III}]_2$	μ-η^2:η^2 $[Fe^{III}]_2$
Fe1−Fe2	3.68	4.28	3.68	3.67
O3−O4	1.33	1.36	1.32	1.44
Fe1−O3	1.92	1.87	1.91	1.96
Fe1−O4	2.89	2.76	2.91	2.01
Fe2−O3	2.84	2.53	2.82	2.11
Fe2−O4	1.92	1.89	1.93	2.12
$Fe1-O_{a,D/E84}$	2.18	2.24	2.10	2.28
$Fe1-O_{b,D/E84}$	2.25	2.16	2.40	2.15
$Fe2-O_{a,E204}$	2.28	2.10	1.91	1.93
$Fe2-O_{b,E204}$	2.13	2.36	3.18	3.44
E(rel to $[Fe^{II}]_2$) (kcal/mol)	−24.6	−14.4	−26.0	−15.9

R2-W48F/D84E peroxo intermediate and the $[Fe^{III}_2(O_2)(OBz)_2\{HB(pz')_3\}_2]$ model complex.

3.2.2. R2-W48F/D84E Peroxo Models. To evaluate possible peroxide binding modes of the R2-W48F/D84E and R2-wt peroxo species, spin-unrestricted broken-symmetry ($M_S = 0$) DFT geometry optimizations were performed on several hypothetical active site models that were based on the X-ray structure of reduced R2-wt and the R2-W48F/D84E variant.[64] Geometry optimizations utilizing a variety of initial geometries resulted in two distinct peroxo binding geometries for both the W48F/D84E- and R2-wt models. The R2-W48F/D84E model generated either a *cis* μ-1,2 peroxo $[Fe^{III}]_2$ dimer or a *trans* μ-1,2 peroxo $[Fe^{III}]_2$ structure depending on the starting geometry used in the optimization (Figure 5). Total energies and key structural features of the geometry optimized models are summarized in Table 8, and the compositions of the Fe 3d-based unoccupied molecular orbitals (MOs) are given in Tables 9 and 10. Both irons are 6C with bidentate terminal carboxylates.

Fe−peroxide bonding is spread among four MOs in the R2-W48F/D84E *cis* μ-1,2 peroxo $[Fe^{III}]_2$ complex, with the occupied peroxo π^*_π and π^*_σ orbitals overlapping with the iron d-orbitals. π^*_π is the dominant donor, forming a π-overlap with two of these orbitals: *yz* (Figure 6b, 25% π^*_π) and $x^2 - y^2$ (Figure 6a, 11% π^*_π). The π^*_σ forms a σ-bond with the z^2 orbital (Figure 6c, 11% π^*_σ) and *xz* (Figure 6b, 9% π^*_σ). This bonding motif is similar to that computed for the $[Fe^{III}_2(O_2)(OBz)_2\{HB(pz')_3\}_2]$ model complex (Table 7). This indicates that the bonding in *cis* μ-1,2 peroxo $[Fe^{III}]_2$ complexes is dominated by peroxo-Fe^{III} bonding. While the qualitative bonding pattern is the same for both the synthetic model complex and the double variant *cis* μ-1,2 peroxo structure, there is an important quantitative difference. The total peroxo donor strength in the R2-W48F/D84E *cis* μ-1,2 structure is 6% less than that calculated for $[Fe^{III}_2(O_2)(OBz)_2\{HB(pz')_3\}_2]$. This difference is attributed to the different terminal ligands present in the two species; $[Fe^{III}_2(O_2)(OBz)_2\{HB(pz')_3\}_2]$ is modeled with amine ligands, while the R2-W48F/D84E *cis* μ-1,2 peroxo is capped by a histidine and an anionic carboxylate residue. As a result, the relative amount of endogenous ligand donation in the two structures is 11% greater for the protein model (36% vs 25%). Experimental support for these computational results comes from the lower O_2^{2-} charge-transfer intensity and weaker Fe−O stretching force constant in the protein intermediate relative to the model complex.

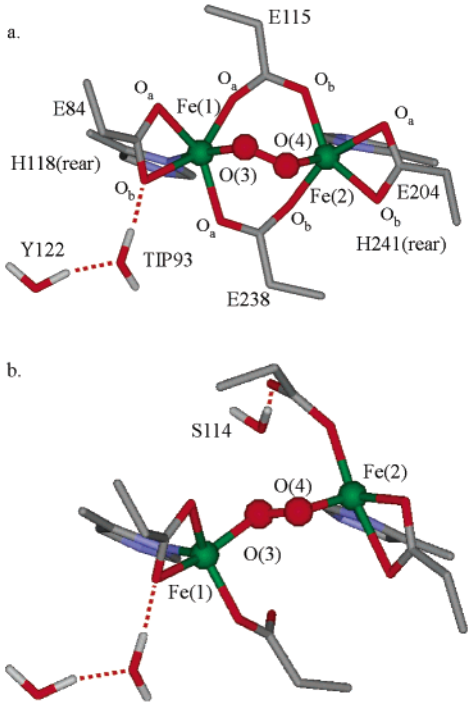

Figure 5. Geometry optimized structures. (a) *cis* μ-1,2-peroxo $[Fe^{III}]_2$ and (b) *trans* μ-1,2-peroxo $[Fe^{III}]_2$ structures of R2-W48F/D84E. Hydrogens and some hydrogen-bonding residues are omitted for clarity (full model in the Supporting Information). S114 is included in all computations but only shown in part b for clarity.

Table 9. Compositions of the Unoccupied Fe1 3d-Derived MOs for the R2-W48F/D84E *cis* μ-1,2-Peroxo; Model Obtained from Spin-Unrestricted BS ($M_S = 0$) Calculations[63]

E (eV)	orb no.	orb	N′, O′	Fe1	O3	O4	peroxo orb	Fe2	N′, O′
−2.176		z^2	32	49	6	2	π^*_σ	0	0
−2.796		*xy*	20	75	0	0		0	0
−3.401		*yz*	1	57	20	11	π^*_π	2	0
−3.553		x^2-y^2	4	80	4	3	π^*_π	0	0
−3.727	LUMO	*xz*	0	82	6	3	π^*_σ	0	0
total peroxo character in Fe 3d-based MOs				36 + 21			= 57%		

[a] Coordinate system (for Fe1): z = Fe2−O_{peroxo} bond vector, $x \approx$ Fe2−$O_{a,E84}$ bond, $y \approx$ Fe2−$O_{b,E84}$ bond.

(63) Fe1-based unoccupied 3d-orbitals are shown, Fe2-centered are similar (<5% difference) and are found in the Supporting Information.

(64) It is of interest to note that reduced R2 under crystallization conditions will react with O_2. In contrast, biferrous MMO crystal structures are of the hydroxylase protein (MMOH) which reacts haltingly with O_2 relative to when the effector protein, MMOB, is also present. Thus, the structure of the reactive biferrous MMO species remains unknown.

Table 10. Compositions of the Unoccupied Fe1 3d-Derived Unoccupied MOs for the R2-W48F/D84E *trans* μ-1,2-Peroxo; Model Obtained from Spin-Unrestricted BS ($M_S = 0$) Calculations[63]

							peroxo		
E (eV)	orb no.	orb	N′, O′	Fe1	O3	O4	orb	Fe2	N′, O′
−2.780		*xz*	12	66	9	4	π^*_σ	0	0
−3.695		*yz*	10	69	7	4	π^*_π	0	0
−3.965		*xy*	3	68	15	8	π^*_π	0	0
−4.290		x^2-y^2	8	81	0	0		0	0
−4.477	LUMO	z^2	0	79	5	3	π^*_σ	0	0
total peroxo character in Fe 3d-based MOs			36 + 19				= 55%		

[a] Coordinate system: $z \approx$ bisects Fe−O_{peroxo} and Fe−N_{His} bond vectors, and $x \approx$ bisects Fe−O_{peroxo} and Fe−$O_{a,E238}$ bond vectors.

The Fe_2O_2 core geometry of the R2-W48F/D84E *cis* μ-1,2 peroxo $[Fe^{III}]_2$ model is also similar to that of the geometry optimized truncated model of the synthetic $[Fe^{III}_2(O_2)(OBz)_2\{HB(pz')_3\}_2]$ complex. They have similar O−O bond lengths, 1.33 and 1.32 Å, respectively, while the Fe−O bond lengths of the protein structure are slightly longer than those of the model complex (1.92 Å vs 1.88 Å). The model complex core is flattened relative to the protein structure, with the Fe−O−O angle increasing from 123° to 129°, and the Fe−Fe distance increasing from 3.68 to 4.00 Å in the $[Fe_2O_2(O_2CH)_2(NH_3)_6]^{2+}$ model. This angular change results in a lower ν_{O-O} stretching frequency without changing k_{O-O} due to different mechanical coupling of the Fe−O and O−O motions in the two geometries.

The second peroxo structure identified using the constraints of the R2-W48F/D84E protein pocket has a *trans* μ-1,2 peroxo $[Fe^{III}]_2$ structure (Figure 5b). Unlike the *cis* μ-1,2 structure (Figure 5a), for which the endogenous ligand coordination is similar to that of the biferrous species (Chart 1a), the *trans* μ-1,2 peroxo is greatly distorted, with the two bridging carboxylate ligands changing to a terminal monodentate coordination on different irons. The Fe_2O_2 core is expanded to accommodate the *trans*-peroxo ligation (r(Fe−Fe) = 4.28 Å, as compared to r(Fe−Fe) = 3.68 Å for the R2-W48F/D84E *cis* μ-1,2 peroxo), resulting in the two previously bridging carboxylates becoming monodentate to Fe1 (E238) and Fe2 (E115). The loss of two coordination bonds to the biferric center from E238 and E115 is compensated for by the two terminal carboxylates forming strong bidentate interactions with the metals. The resulting structure has two 5C irons in a highly distorted square pyramidal ligand field dominated by the Fe−O_{peroxo} and adjacent Fe−$O_{terminal\ carboxylate}$ interactions. Both the peroxo π^*_π and π^*_σ orbitals are involved in bonding to the iron, and each d-orbital has a combination of peroxo and endogenous ligand contributions, resulting in a complicated bonding scheme and reflecting the asymmetric coordination environment.

ΔE for the binding of dioxygen to the biferrous R2-W48F/D84E structure identified previously[35] (Chart 1a) is calculated to be −24.6 kcal/mol for the *cis* μ-1,2 peroxo $[Fe^{III}]_2$ model and −14.4 kcal/mol for the *trans* μ-1,2 peroxo $[Fe^{III}]_2$ structure, resulting in a 10.2 kcal/mol energetic preference for the *cis* μ-1,2 structure. This energy difference is related to differences in the number and relative strengths of bonds in the two structures. The bonding in the Fe_2O_2 core is stronger in the *cis* μ-1,2 model as reflected in the total peroxo donation (60% in *cis* μ-1,2 and 52% in *trans* μ-1,2 (average per iron)). In addition, the *cis* μ-1,2 model consists of two 6C ferric irons, while *trans* μ-1,2 peroxo contains two 5C centers. This net loss of two bonds acts to destabilize the latter model as the charge on the ferric irons is less well distributed over the ligands, although this effect is somewhat reduced by the shorter Fe1−O_{E238} and Fe2−O_{E115} bonds relative to the *cis* μ-1,2 model. These structural differences have energetic consequences, which make the *cis* μ-1,2 peroxo structure a much more favorable R2-W48F/D84E peroxo intermediate model. This conclusion is supported by our experimental data on the protein intermediate, as the *trans* structure requires an unreasonably weak k_{Fe-O} in order to reproduce the observed rR spectrum.

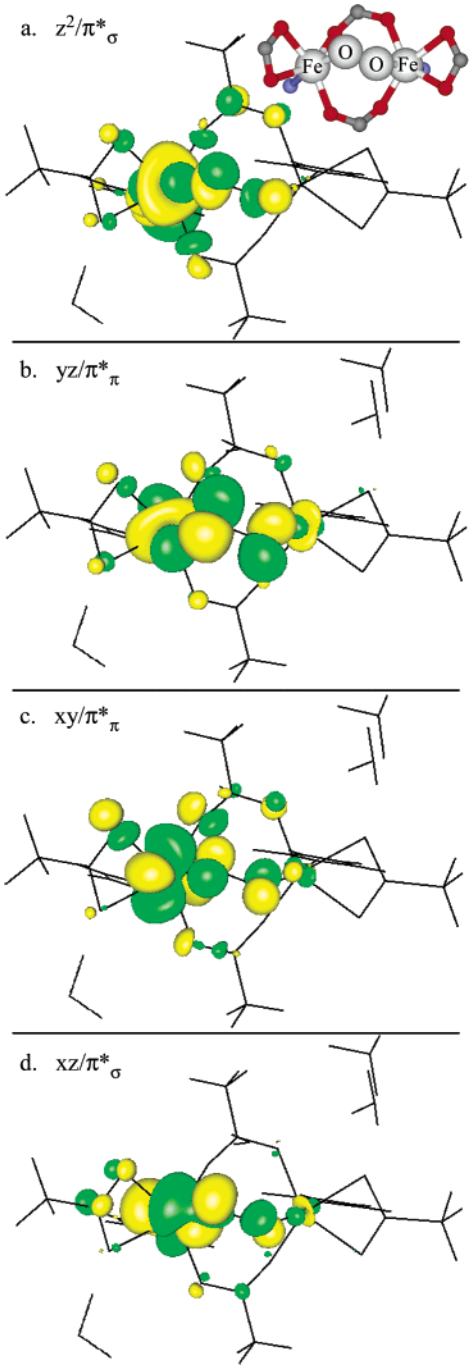

Figure 6. Surface plots of the peroxide bonding orbitals from a truncated version of the R2-W48F/D84E *cis* μ-1,2-peroxo model (Figure 5a) obtained from an SU-BS ADF calculation. (a) z^2/π^*_σ (Inset: cartoon of Fe coordination for reference), (b) yz/π^*_π, (c) xy/π^*_π, and (d) xz/π^*_σ. Coordinate system (for Fe1): z = Fe1−O_{peroxo} bond vector, $x \approx$ Fe2−$O_{a,\ E204}$ bond, $y \approx$ Fe−$O_{b,\ E204}$ bond.

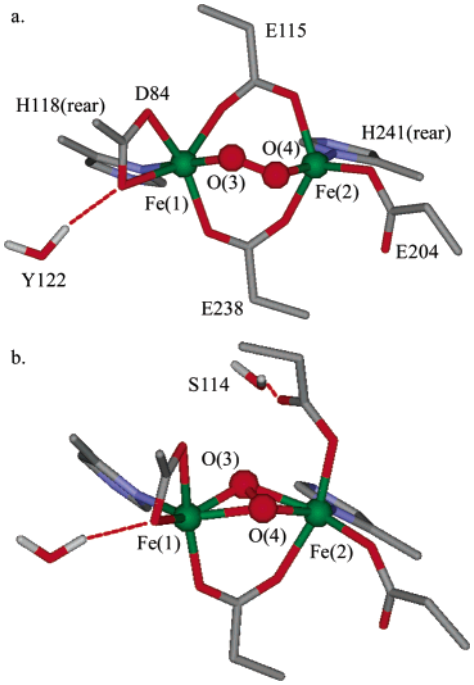

Figure 7. Geometry optimized structures. (a) *cis* μ-1,2-peroxo $[Fe^{III}]_2$ and (b) μ-η^2:η^2 peroxo $[Fe^{III}]_2$ structures of R2-wt. Hydrogens and some hydrogen-bonding residues are omitted for clarity (full model in the Supporting Information). S114 is included in all computations but is only shown in part b for clarity. Carboxylate oxygen atom labels are the same as those shown in Figure 5a.

Table 11. Compositions of the Unoccupied Fe1 3d-Derived Unoccupied MOs for the R2-wt *cis* μ-1,2-Peroxo; Model Obtained from SU-BS ($M_S = 0$) Calculations[63]

							peroxo		
E (eV)	orb no.	orb[a]	N′, O′	Fe1	O3	O4	orb	Fe2	N′, O′
−2.160		z^2	15	63	7	4	π^*_σ	0	0
−3.061		xy	15	77	0	0		0	0
−3.552		yz	0	50	24	15	π^*_π	3	0
−3.804		x^2-y^2	0	88	0	0		0	0
−3.876	LUMO	xz	0	75	7	5	π^*_π	2	0
total peroxo character in Fe 3d-based MOs				38 + 24			= 62%		

[a] Coordinate system (for Fe1): z = Fe1−O_{peroxo} bond vector, $x \approx$ Fe1−$O_{a,E115}$ bond, $y \approx$ Fe1−$O_{a,D84}$ bond.

3.2.3. R2-wt Peroxo Models. The same approach as that outlined in section 3.2.2 was used to explore geometries of peroxo structures using the constraints of the R2-wt protein. The R2-wt model converged to either a *cis* μ-1,2 peroxo $[Fe^{III}]_2$ dimer similar to that obtained for the R2-W48F/D84E variant or a side-on μ-η^2:η^2 peroxo $[Fe^{III}]_2$ dimer (Figure 7). Total energies and key structural features of the geometry optimized models are summarized in Table 8, and the compositions of the Fe1 3d-based unoccupied molecular orbitals (MOs) are given in Table 11.

The *cis* μ-1,2 peroxo $[Fe^{III}]_2$ model (Figure 7a) generated using the protein constraints for R2-wt is similar to that from R2-W48F/D84E in terms of both its geometry and electronic structure description. Fe1 is labeled as 6C due to an asymmetric bidentate D84 carboxylate ligation (Fe−O_{D84} distances of 2.09 and 2.40 Å), while Fe2 is 5C with E204 clearly monodentate with one 1.91 Å and one 3.81 Å Fe−O_{E204} distance. The Fe_2O_2 cores in R2-wt and R2-W48F/D84E peroxo intermediates have nearly identical Fe−O and O−O bond lengths (Table 8), and the calculated total peroxide donation is similar (R2-W48F/D84E *cis* μ-1,2 peroxo: 57%(Fe1) + 56%(Fe2) = 113%. R2-wt *cis* μ-1,2 peroxo: 62%(Fe1) + 57%(Fe2) = 119%). R2-wt peroxo has three principle bonding interactions, involving *xz* (11% π^*_π), *yz* (32% π^*_π) and z^2 (12% π^*_σ). The *yz* and z^2 orbitals are similar in appearance to those of the R2-W48F/D84E *cis* μ-1,2 peroxo shown in Figure 6. The distribution of peroxo donation into the Fe d-manifold differs from that in the R2-W48F/D84E structure as the coordination geometry at Fe2 in the R2-wt *cis* μ-1,2 peroxo is 5C trigonal bipyramidal, while the corresponding R2-W48F/D84E species is 6C octahedral.

Table 12. Compositions of the Unoccupied Fe 3d-Derived Unoccupied MOs for the R2-wt μ-η^2:η^2 Peroxo Model Obtained from Spin-Unrestricted BS ($M_S = 0$) Calculations (Both the Fe1- and Fe2-Based Orbitals Are Shown Due to the Marked Asymmetry in the Bonding)

Fe1-based d-orbitals

							peroxo		
E (eV)	orb no.	orb[a]	N′, O′	Fe1	O3	O4	orb	Fe2	N′, O′
−2.831		x^2-y^2	7	61	14	14	π^*_σ	0	0
−3.021		z^2	14	76	3	0		0	0
−3.950		xy	2	77	1	2		0	0
−4.073		xz	2	70	9	2	π^*_π	0	0
−4.281	LUMO	yz	2	74	4	13	π^*_π	0	0
total peroxo character in Fe 3d-based MOs				31 + 31			= 62%		
average peroxo donation over dimer				22/2 + 62/2 = 42% per iron					

Fe2-based d-orbitals

							peroxo		
E (eV)	orb no.	orb[a]	N′, O′	Fe1	O3	O4	orb	Fe2	N′, O′
−2.944		z^2	0	0	7	0	π^*_σ	69	11
−3.041		x^2-y^2	0	0	3	9	π^*_σ	68	7
−3.975		xy	0	0	1	0		80	9
−4.126		xz	0	0	0	0		81	9
−4.216	LUMO	yz	0	0	0	2		81	8
total peroxo character in Fe 3d-based MOs				11 + 11			= 22%		

[a] Coordinate system (for Fe1): $x \approx$ Fe1−O4 bond vector, $y \approx$ Fe1−O3 bond vector, z = perpendicular to FeO_2 plane. Fe2: $x \approx$ Fe1−O3 bond vector, $y \approx$ Fe1−O4 bond vector, z = perpendicular to FeO_2 plane.

R2-wt μ-η^2:η^2 peroxo (Figure 7b) is a distorted butterfly structure with short Fe−O bonds to Fe1 (1.96 and 2.01 Å) and long Fe−O bonds to Fe2 (2.11 and 2.12 Å). During the convergence to the butterfly structure, the Fe1−E115 bond length gradually increases, which allowed E115 to swing out and hydrogen bond with the hydroxide of S114. In the final geometry, each iron is 6C. Fe1 is monodentate coordinated to H118 and E238, while D84 and the peroxide are bidentate. Fe2 also forms two bonds to the peroxide and coordinates the four adjacent residues (E115, E204, E238, and H241) in a monodentate configuration. This geometry differs from the *trans* μ-1,2-peroxo structure obtained using the R2-W48F/D84E protein constraints and a similar ((6C,6C), μ-η^2:η^2) starting geometry (Figure 5b). The presence of significant steric strain in this geometry is evidenced by the butterfly (nonplanar) structure. With R2-W48F/D84E constraints, this strain is large enough to break the Fe2−O_{E238} bond, allowing the Fe_2O_2 core to expand to the final *trans* μ-1,2-peroxo structure. The stronger bonding between the peroxo and Fe1 than Fe2 is reflected in the total peroxo donation to each metal (Table 12). Fe1 has 62% peroxo character, while Fe2 has 22%. The primary bonding interaction between peroxide and Fe1 involves sigma overlap between the x^2-y^2 and π^*_σ orbitals (the x and y axes point roughly along the two Fe−O_{peroxo} bonds). There is also overlap

Chart 5. Oxygen Activation Pathway Involving Asymmetric Cleavage of O−O Bond to Form a High-Valent μ-Oxo Structure

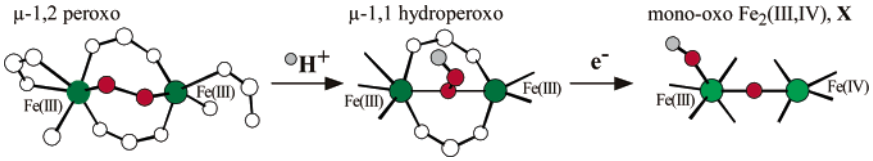

between Fe1 and the peroxo π^*_π orbital. Fe−O bond length asymmetry results in the peroxo π^*_π donation being distributed among the d-manifold, with one atom (O3) donating to the *yz* orbital, while the other (O4) donates to *xz*. For Fe2, however, the longer Fe−O bonds result in net peroxo donation being much smaller, with the only significant interaction being peroxo π^*_σ donation to the Fe2 x^2-y^2 orbital.

The optimized O−O distance in μ-η^2:η^2 peroxo is much longer (1.44 Å) than that obtained for the μ-1,2 structures (1.32 Å). This lengthening derives from the decreased peroxo donation into the Fe d-manifold, as the total peroxo donation per iron is 42%, significantly less than the 57% observed for the R2-wt *cis* μ-1,2 peroxo. This decreased donation from the peroxo π* orbitals weakens the O−O bond and results in a longer bond relative to the μ-1,2 coordination mode.

The calculated energetics of biferric peroxo formation from biferrous R2-wt are −26.0 kcal/mol for the R2-wt *cis* μ-1,2 peroxo structure (Figure 7a) and −15.9 kcal/mol for the μ-η^2:η^2 peroxo (Figure 7b), resulting in the *cis* μ-1,2 peroxo being −10.1 kcal/mol more stable. This energy difference is due to steric strain, weak peroxo donation, and breaking of the Fe1−O_{E115} bond. Placing a μ-η^2:η^2 Fe_2O_2 unit within the protein-constrained active site pocket of R2 results in a steric clash between the two iron atoms and the terminal ligands. To relieve this strain, the typically planar μ-η^2:η^2 Fe_2O_2 core[65] bows to form a butterfly structure (Figure 7b), bringing the two irons closer together. This butterfly distortion also leads to poor net overlap between the iron d-orbitals and the peroxo orbitals, which results in the decrease in net peroxo donation. The third factor is the loss of the Fe1−O_{E115} bond upon adopting a butterfly structure. This results in the *cis* μ-1,2 peroxo coordination mode being the most energetically favorable for this model of the constraints of the R2-wt active site pocket.

4. Discussion

4.1. Relationship of R2-W48F/D84E *cis* μ-1,2-Peroxo to the $[Fe^{III}_2(O_2)(OBz)_2\{HB(pz'_3)_2\}]$ Model Complex. Analysis of absorption and rR spectra along with rR excitation profiles reveal that only the *cis* μ-1,2 peroxo structure is compatible with our experimental data, whereas other coordination motifs can be discounted on the basis of our NCA. While the R2-W48F/D84E peroxo intermediate and $[Fe^{III}_2(O_2)(OBz)_2\{HB(pz'_3)_2\}]$ are qualitatively similar, analysis of the relative intensities of the ∼14 000 cm^{-1} peak in their absorption spectra indicates that the ratio of peroxo charge donation in the protein relative to the model is 0.56 (Table 2). This reduced donor strength of the peroxo ligand in the protein environment is consistent with DFT calculations, which show that the lower peroxo charge donation to iron is accompanied by an increase in the endogenous ligand donation in the protein site (25% vs 36% endogenous ligand contribution to the Fe d-manifold).

The peroxo charge donation in the $[Fe^{III}_2(O_2)(OBz)_2\{HB(pz'_3)_2\}]$ model complex is similar to that of μ-1,2 peroxo Cu^{2+} dimers.[32] The peroxide in these copper dimers was shown experimentally to be relatively basic,[66] indicating that the peroxo of the R2-W48F/D84E peroxo intermediate, with its smaller peroxo donation, is even more basic. This suggests that the peroxo becomes more nucleophilic in the protein environment and is activated for attack by adjacent electrophiles. The prime candidate for such a reaction is water, which could donate a proton to the peroxo unit to form a hydroperoxide. There are 10 water molecules identified to be within 10 Å of the binuclear iron center in the crystal structure of oxidized R2, indicating that water is not excluded from the active site environment and is available to react with the peroxo intermediate. Hydroperoxo is a weaker donor than peroxo, which would weaken the Fe^{III}−O bond on the protonated end of the hydroperoxide bridge. Such a species may be activated to undergo isomerization to a μ-1,1 hydroperoxo (Chart 5) followed by cleavage of the O−O bond, generating a high-valent mono-μ-oxo-bridged species similar to that anticipated by ENDOR[20] and consistent with MCD[21] studies of intermediate **X**.

4.2. Relationship of Spectroscopically Calibrated DFT Structures to Protein Intermediates. 4.2.1. R2-wt Peroxo. This study reveals that only a *cis* μ-1,2-peroxo coordination geometry is compatible with the experimental data for the R2-W48F/D84E peroxo intermediate. This structure is geometrically and electronically analogous to the R2-wt *cis* μ-1,2-peroxo model identified computationally. A peroxo intermediate has not been definitively characterized in stopped-flow experiments using R2-wt, suggesting that kinetic masking of this intermediate may be occurring, where its decay is much faster than its formation. The product of the R2-wt reaction pathway, the stable tyrosine radical, $Y122^\bullet$, is also formed in the R2-D84E variant. The crystallographically defined active site of R2-D84E closely overlays that of the R2-W48F/D84E double variant, with the mutated residue, 48, located ∼9 Å from the binuclear iron center. The W48F substitution does not perturb the geometry of the binuclear active site appreciably, leading to formation of nearly identical peroxo intermediates in the single and double variant. Thus, a μ-1,2-peroxo intermediate is also generated in R2-D84E, a protein that forms the same ultimate product as R2-wt. This hypothesis is consistent with the results of the modeling study presented above, suggesting that the initial peroxo intermediate of R2-wt also has a *cis* μ-1,2-peroxo geometry.

Other geometries have been advocated for the putative R2-peroxo intermediate based upon DFT geometry optimizations using a variety of DFT methods and active site models. Some propose a μ-η^2:η^2 peroxo coordination geometry,[28,54] while

(65) Henson, M. J.; Mukherjee, P.; Root, D. E.; Stack, T. D. P.; Solomon, E. I. *J. Am. Chem. Soc.* **1999**, *121*, 10332−10345.

(66) Fox, S.; Karlin, K. D. In *Active Oxygen in Biochemistry*; Valentine, J. S., Foote, C. S., Greenberg, A., Liebman, J. F., Eds.; Blackie Academic & Professional: Glasgow, 1995.

others favor a *cis* μ-1,2 geometry.[67] The computational approach used in these studies differs from that utilized in this paper (section 2.3) in two major respects: (i) the coordinating amino acid residues are not constrained at their α-carbon positions and (ii) the hydrogen-bonding residues in the second coordination sphere with high protein field interaction energies[12] were not included, thus ignoring the limitations on ligand position imposed by the tertiary protein structure. These steric and electrostatic constraints have been shown to be required in order to reproduce the active site geometry of the biferrous sites of binuclear iron enzymes.[12,35,36] Although freezing atomic coordinates removes any flexibility in the protein tertiary structure, this constrained approach is excellently suited to the investigation of oxygen activation in R2 as evidenced by the fact that the lowest energy peroxo intermediate structure agrees well with spectroscopic data. However, it is important to note that results gained from truncated computational models including those presented in this study should be considered only with close reference to experimental observables.

Studies of the early oxygen activating intermediates in R2-W48A/D84E (a variant that has the same O_2 intermediates as R2-W48F/D84E) have been performed using chemical mediation of electron transfer (CMET) by substituted indoles.[68,69] These have found that CMET of the R2-W48A/D84E peroxo intermediate results in formation of Y122$^\bullet$, but that this increases the rate of peroxo decay by only 20%. This suggests that an additional transformation of the biferric peroxo intermediate is required prior to CMET (i.e., reduction) and formation of **X**.

Similar experiments on R2 variants with the R2-wt iron-coordinating ligand set (R2-W48A/Y122F) identify an intermediate that exists prior to the formation of **X**.[68,69] This species displays Mössbauer[70] and absorption[71] features different from those of a biferric μ-1,2-peroxo geometry. As an initial proposal, we suggest that this may be a protonated peroxo species. The weak absorption features relative to the biferric μ-1,2-peroxo are consistent with the changes observed between Cu(II)-peroxo/Cu(II)-hydroperoxo, where protonation weakens the electron affinity of the peroxide and reduces its donor strength.[72−74] A simulation of the Mössbauer data had fit parameters consistent with an asymmetric μ-1,2-hydroperoxo geometry where one iron is coordinated to the oxo, while the other is coordinated to the more weakly coordinating hydroxo end of the hydroperoxo ligand.[75]

Thus, R2 variants with the W48A substitution and either the wild-type iron-coordinating ligand set (R2-W48A/Y122F) or the D84E substitution (R2-W48A/D84E) are competent to form the tyrosine radical, Y122$^\bullet$, upon CMET. Additionally, the R2-W48A/D84E biferric μ-1,2-peroxo intermediate converts to a species that forms Y122$^\bullet$, upon CMET. These observations, combined with the present study, suggest that the reaction mechanisms of variants with the R2-wt iron-coordinating residues or the D84E mutation are similar, but that there are different relative rates between individual reaction steps in R2-W48A/D84E and R2-W48A/Y122F. The biferric μ-1,2-peroxo intermediate of R2-W48A/Y122F may form an initial biferric μ-1,2-peroxo intermediate as identified by the calculations and be rapidly protonated before freeze-quenching, forming the intermediate observed by Bollinger and co-workers.[69] The R2-W48A/D84E variant also forms a μ-1,2-peroxo intermediate as described in this manuscript, but this intermediate is relatively long-lived, and the formation of **X** is not greatly accelerated by the addition of rescuing agent. This transformation is proposed to be the same peroxide protonation step which is rapid in R2-W48A/Y122F but greatly slowed in R2-W48A/D84E due to structural differences within the active sites in the two variants.

4.2.2. MMO−P. As described in section 1, the spectroscopic signatures of intermediate **P** of MMO are very similar to those of the peroxo intermediates of R2-D84E, R2-W48F/D84E, and Δ9D, which have been shown to possess a μ-1,2-peroxo geometry. In contrast, repeated DFT investigations of the reaction mechanism of O_2 activation in MMO have presented a variety of structures for **P**, depending upon the size of the model and the level of theory used. [2] Proposed core structures include the μ-η^2:η^2,[54,76] the μ-η^1:η^2,[28,36] the *trans* μ-1,2[28] and the *cis* μ-1,2 geometries.[77,78] The currently preferred structure for **P** is the μ-η^2:η^2 biferric peroxo structure,[27,54] a starting point from which homolytic cleavage of the O−O bond forms the experimentally supported bis-μ-oxo $Fe^{IV}Fe^{IV}$ structure that has been proposed for **Q**.[26] These calculations are based upon X-ray crystal structures of biferrous MMOH (the hydroxylase component of MMO), which is observed to have limited oxygen reactivity[79] and to change structure once MMO component B is permitted to bind.[80,81] Although the μ-η^2:η^2 coordination geometry is energetically disfavored in our computational model of the R2-W48F/D84E active site, it is not definitively eliminated as a candidate for **P** as hydrogen-bonding from residues in the second coordination sphere are vital to reproducing the active site geometry observed crystallographically,[11,35,36] and these hydrogen-bonding interactions differ between MMO and R2.[12] However, it is difficult to rationalize the strikingly similar electronic absorption spectra and Mössbauer parameters of **P** and the R2-W48F/D84E peroxo intermediate if the peroxide binding mode were fundamentally different.

4.2.3. Hemerythrin. Hemerythrin (Hr) is a binuclear non-heme iron oxygen transport protein found in invertebrates.[82] It has two physiologically relevant forms, the biferrous (deoxyHr) and the hydroperoxide biferric (oxyHr). deoxyHr has one 5C (Fe1) and one 6C (Fe2) iron linked by two μ-1,3 carboxylate

(67) Torrent, M.; Musaev, D. G.; Basch, H.; Morokuma, K. *J. Comput. Chem.* **2002**, *23*, 59−76.
(68) Saleh, L.; Kelch, B.; Pathickal, B.; Baldwin, J.; Ley, B.; Bollinger, J. *Biochemistry*, submitted.
(69) Saleh, L.; Krebs, C.; Ley, B.; Naik, S.; Huyhn, B.; Bollinger, J. *Biochemistry*, submitted.
(70) A broad doublet at ∼0.3 and 0.8 mm/s and a sharper doublet at ∼ −0.3 and 1.2 mm/s.
(71) A low intensity peak at ∼500 nm (ϵ < 100/M/cm).
(72) Solomon, E.; Lowery, M.; Root, D.; Hemming, B. *Mech. Bioinorg. Chem.* **1995**, *246*, 121−164.
(73) Solomon, E.; Tuczek, F.; Root, D.; Brown, C. *Chem. Rev.* **1994**, *94*, 827−856.
(74) Root, D.; Mahroof-Tahir, M.; Karlin, K.; Solomon, E. *Inorg. Chem.* **1998**, *37*, 4838−4848.
(75) This fit identified two intermediate species in equilibrium prior to formation of **X**, one with inequivalent irons and one with equivalent irons. Their parameters were as follows: inequivalent: ($\Delta E_Q(1) = 1.53$ mm/s, $\delta(1) = 0.45$ mm/s) and ($\Delta E_Q(2) = 0.53$ mm/s, $\delta(2) = 0.60$ mm/s); equivalent ($\Delta E_Q = 0.55$ mm/s, $\delta = 0.43$ mm/s).
(76) Yoshizawa, K.; Ohta, T.; Yamabe, T.; Hoffmann, R. *J. Am. Chem. Soc.* **1997**, *119*, 12311−12321.
(77) Torrent, M.; Musaev, D. G.; Morokuma, K. *J. Phys. Chem. B* **2001**, *105*, 322−327.
(78) Yoshizawa, K.; Yokomichi, Y.; Shiota, Y.; Ohta, T.; Yamabe, T. *Theor. Chem. Lett.* **1997**, 587−591.
(79) Lipscomb, J. D.; Que, L. *J. Biol. Inorg. Chem.* **1998**, *3*, 331−336.
(80) Pulver, S.; Froland, W.; Lipscomb, J.; Solomon, E. *J. Am. Chem. Soc.* **1997**, *119*, 387−395.
(81) Pulver, S.; Froland, W.; Fox, B.; Lipscomb, J.; Solomon, E. *J. Am. Chem. Soc.* **1993**, *115*, 12409−12422.
(82) Stenkamp, R. E. *Chem. Rev.* **1994**, *94*, 715−726.

bridges and one μ-OH ligand that faces the oxygen binding pocket. The remaining three ligands on the 6C iron and the two other ligands on the 5C are all histidines.[83] O_2 binding begins with one oxygen coordinating to Fe1 of deoxyHr to form a (6C, 6C) binuclear site. A proton coupled electron transfer (PCET) then occurs along the reaction coordinate with the proton of the bridging hydroxide tunneling to the uncoordinated oxygen atom coupled to electron transfer through a superexchange pathway from Fe2 to oxygen via the nascent oxo bridge.[84] The second electron is transferred to O_2 from Fe1, generating a hydroperoxo ligand bound to the exchange-coupling stabilized μ-oxo Fe^{III}_2 unit. The two-electron reduction of O_2 to peroxide via a monodentate, nonbridging coordination mode is thus achieved through the presence of the oxo bridge which allows for strong superexchange pathways between the two metal centers. Electron transfer dominantly occurs through this pathway as the μ-1,3 carboxylate bridges form weak superexchange pathways[2,84] and the Fe1−Fe2 distance, 3.50 Å, is too large for direct electron transfer.

The biferrous site of R2 and its variants are bridged by two μ-1,3 carboxylates, but unlike deoxyHr, it is not believed to form an oxo bridge along the reaction coordinate of O_2 binding to form the peroxo−biferric intermediate. The coordination of dioxygen to one iron could result in the transfer of one electron from Fe1 to O_2 to form a superoxide, but there would be a sizable kinetic barrier to transfer the second electron from the remote iron to O_2 as the carboxylates are poor electron-transfer conduits and the long Fe−Fe distance (~3.90 Å) prevents direct electron transfer. In contrast to deoxyHr, however, the biferrous state of the binuclear non-heme iron enzymes contains two coordinatively unsaturated ferrous ions (a (5C, 4C) site in the case of R2-wt). This permits the *cis* μ-1,2 peroxo bridging coordination observed experimentally in the binuclear non-heme iron enzymes, with one electron being transferred directly from each iron to O_2 to form a bridging peroxide and initiate oxygen activation for catalysis.

(83) Holmes, M.; Le Trong, I.; Turley, S.; Siekler, L.; Stenkamp, R. *J. Mol. Biol.* **1991**, *218*, 583−593.
(84) Brunold, T. C.; Solomon, E. I. *J. Am. Chem. Soc.* **1999**, *121*, 8288−8295.

5. Summary

The coordination geometry of the R2-W48F/D84E peroxo intermediate has been experimentally shown to possess a biferric *cis* μ-1,2 peroxo core structure. This assignment is supported by DFT geometry optimizations using the constraints imposed on the R2-W48F/D84E active site ligand set, which identify a *cis* μ-1,2 peroxo as the most stable peroxo intermediate structure. Applying this active site modeling approach to the putative peroxo intermediate of R2-wt finds that the preferred structure is also *cis* μ-1,2 with a similar electronic structure to the experimentally validated structure of the R2-W48F/D84E peroxo. This bridging mode allows two-electron reduction of O_2 by the binuclear iron center. The geometric and electronic structures of both wt- and double-variant-R2 *cis* μ-1,2 peroxo models suggest that the presence of anionic iron-coordinating ligands in the active site decreases the peroxo charge donation and enhances peroxo nucleophilicity for subsequent reactivity. Although the data for MMO-**P** resemble those for the R2 variant peroxo intermediates, the presence of different hydrogen-bonding residues in the second coordination sphere prevent generalization of our results to other proteins. In contrast, the differing functions of the oxygen transport protein, Hr, and the oxygen activating enzymes are understood by noting the lack of an oxo bridge in the peroxo biferric intermediate species in R2, a structure that contributes to the driving force for the generation of high-valent oxo-bridged intermediates for reactivity.

Acknowledgment. Financial support by the NSF-Biophysics Program Grant MCB 9214214 (E.I.S.), NIH GM55365 (J.M.B., Jr.)

Supporting Information Available: NCA model coordinates, 2.5 Å Fe−Fe separation *cis* μ-1,2 model NCA results, DFT calculation coordinates, full W48F/D84E-R2 model figure, Fe d-orbital compositions not included in main body of manuscript. This material is available free of charge via the Internet at http://pubs.acs.org.

JA049106A